

Durham Research Online

Deposited in DRO:

01 March 2017

Version of attached file:

Published Version

Peer-review status of attached file:

Peer-reviewed

Citation for published item:

De Haas, T. and Conway, S. J. and Krautblatter, M. (2015) 'Recent (Late Amazonian) enhanced backweathering rates on Mars : paracratering evidence from gully alcoves.', *Journal of geophysical research : planets.*, 120 (12). pp. 2169-2189.

Further information on publisher's website:

<https://doi.org/10.1002/2015je004915>

Publisher's copyright statement:

de Haas, T., S. J. Conway, and M. Krautblatter (2015), Recent (Late Amazonian) enhanced backweathering rates on Mars: Paracratering evidence from gully alcoves, *Journal of Geophysical Research: Planets*, 120(12), 2169-2189, DOI: 10.1002/2015JE004915. To view the published open abstract, go to <https://doi.org/> and enter the DOI.

Additional information:

Use policy

The full-text may be used and/or reproduced, and given to third parties in any format or medium, without prior permission or charge, for personal research or study, educational, or not-for-profit purposes provided that:

- a full bibliographic reference is made to the original source
- a [link](#) is made to the metadata record in DRO
- the full-text is not changed in any way

The full-text must not be sold in any format or medium without the formal permission of the copyright holders.

Please consult the [full DRO policy](#) for further details.

RESEARCH ARTICLE

10.1002/2015JE004915

Key Points:

- Late Amazonian backweathering rates decrease with crater age
- Late Amazonian backweathering rates are an order of magnitude higher than erosion rates
- Enhanced backweathering rates in gullies suggest liquid water as a catalyst for weathering

Supporting Information:

- Figures S1–S12 and Table S1
- Data Set S1

Correspondence to:

T. de Haas,
t.dehaas@uu.nl

Citation:

de Haas, T., S. J. Conway, and M. Krautblatter (2015), Recent (Late Amazonian) enhanced backweathering rates on Mars: Paracratering evidence from gully alcoves, *J. Geophys. Res. Planets*, 120, 2169–2189, doi:10.1002/2015JE004915.

Received 31 JUL 2015

Accepted 3 NOV 2015

Accepted article online 9 NOV 2015

Published online 12 DEC 2015

Recent (Late Amazonian) enhanced backweathering rates on Mars: Paracratering evidence from gully alcoves

Tjalling de Haas¹, Susan J. Conway², and Michael Krautblatter³
¹Faculty of Geosciences, Utrecht University, Utrecht, Netherlands, ²Department of Physical Sciences, Open University, Milton Keynes, UK, ³Faculty of Civil, Geo and Environmental Engineering, Technical University Munich, Munich, Germany

Abstract Mars is believed to have been exposed to low planet-wide weathering and denudation since the Noachian. However, the widespread occurrence of alcoves at the rim of pristine impact craters suggests locally enhanced recent backweathering rates. Here we derive Late Amazonian backweathering rates from the alcoves of 10 young equatorial and midlatitude craters. The enhanced Late Amazonian Martian backweathering rates (10^{-4} – 10^{-1} mm yr⁻¹) are approximately 1 order of magnitude higher than previously reported erosion rates and are similar to terrestrial rates inferred from Meteor crater and various Arctic and Alpine rock faces. Alcoves on initially highly fractured and oversteepened crater rims following impact show enhanced backweathering rates that decline over at least 10^1 – 10^2 Myr as the crater wall stabilizes. This “paracratering” backweathering decline with time is analogous to the paraglacial effect observed in rock slopes after deglaciation, but the relaxation timescale of 10^1 – 10^2 Myr compared to 10 kyr of the Milankovitch-controlled interglacial duration questions whether a paraglacial steady state is reached on Earth. The backweathering rates on the gullied pole-facing alcoves of the studied midlatitude craters are much higher (~2–60 times) than those on slopes with other azimuths and those in equatorial craters. The enhanced backweathering rates on gullied crater slopes may result from liquid water acting as a catalyst for backweathering. The decrease in backweathering rates over time might explain the similar size of gullies in young (<1 Ma) and much older craters, as alcove growth and sediment supply decrease to low-background rates over time.

1. Introduction

In its early history, during the Noachian period (~4.1–3.7 Ga), Mars was characterized by high rates of geological and fluvial activity, such as impact cratering, erosion, weathering, and valley formation [e.g., Carr and Head, 2010]. At the end of this period, geological and fluvial activity sharply decreased. Phyllosilicates detected from orbit are thought to have been formed by aqueous alteration in the Noachian period, after which sulfates formed in a largely dry, acidic environment [Bibring et al., 2006]. Throughout the Hesperian (3.7–3.0 Ga) and the Amazonian (3.0 Ga up to present) periods, Mars’ surface is thought to have been mainly subjected to very slow surficial weathering without liquid water playing a major role [e.g., Bibring et al., 2006; Chevrier and Mathé, 2007; Ehlmann et al., 2011]. Accordingly, crater denudation rates dropped by 2–5 orders of magnitude after the Noachian and have remained low for the rest of the planet’s history [Golombek et al., 2006, 2014b].

However, relatively high post-Noachian erosion and weathering rates appear to have occurred locally. In the last few million years on Mars (hereafter referred to as Late Amazonian) relatively high erosion and weathering rates have been found in various geological units. Golombek et al. [2014b] found that the rate of erosion of ejecta blocks is ~0.3 m/Myr for craters younger than ~3 Ma. De Haas et al. [2013] found that boulders up to 3 m in diameter shattered into fragments <0.5 m within 1 Myr on a gully fan surface in eastern Promethei Terra. Moreover, De Haas et al. [2013] found that the fan surface relief was smoothed by ~1 m within the same time period. Sand ripple and dune migration rates at the Nili Patera dune field have abrasion rates of 1–10 m/Myr [Bridges et al., 2012]. Young lightly cratered layered deposits on Mars require erosion rates of approximately 1 m/Myr to be free of craters [McEwen et al., 2005], and Grindrod and Warner [2014] inferred similar erosion rates in interior layered deposits from 200 to 400 Ma in Valles Marineris. Enhanced Late Amazonian erosion rates may have resulted from high peak short-term eolian erosion rates [Golombek et al., 2014b]. Moreover, the inferred rates of geologic processes tend to decrease over longer measurement time intervals [Sadler, 1981; Gardner et al., 1987; Golombek et al., 2014b]. For example, the rate of small crater degradation

(infill and erosion) decreased by an order of magnitude when averaged over the last ~20 Ma instead of the last 1 Ma [Golombek *et al.*, 2014b].

The above described denudation rates are mainly inferred from small craters and sedimentary deposits, and erosion can probably be mainly attributed to eolian abrasion [Golombek *et al.*, 2014b]. The only direct estimate of weathering, i.e., the disintegration of rockwalls and rock fragments, stems from boulders on inactive gully fan surfaces [De Haas *et al.*, 2013]. However, rockwall/crater retreat rates are presently unknown on Mars. The widespread presence of alcoves in pristine impact craters [e.g., Reiss *et al.*, 2004; Schon *et al.*, 2009; Hartmann *et al.*, 2010; Johnsson *et al.*, 2014], suggests high local bedrock weathering rates. Alcoves consist of headwall and sidewall escarpments, located below the brink of a slope, and the disrupted topography bounded by these scarps [Malin and Edgett, 2000]. Rockwall weathering and erosion lead to the detachment of bedrock and thereby to the formation of alcoves and associated depositional slopes, aprons, or fans at their base [e.g., Rapp, 1960; André, 1997; Siewert *et al.*, 2012]. Alcoves can be especially large and well developed in Martian midlatitude gullies, where liquid water may have been involved in their formation [e.g., Malin and Edgett, 2000; Dickson and Head, 2009].

Many weathering mechanisms that occur on Earth are hypothesized to have acted on Mars, including salt weathering [e.g., Malin, 1974; Clark and Hart, 1981; Rodriguez-Navarro, 1998; Jagoutz, 2006; Head *et al.*, 2011], insolation or thermal weathering [McFadden *et al.*, 2005; Viles *et al.*, 2010; Eppes *et al.*, 2015], eolian weathering [e.g., Fenton *et al.*, 2005; Bridges *et al.*, 2007; Bourke *et al.*, 2008; Bishop, 2011], and chemical weathering, mainly by acidic volatiles after the Noachian [e.g., Burns, 1993; Banin *et al.*, 1997; Hurowitz and McLennan, 2007; Chevrier and Mathé, 2007]. Moreover, the abundance of fluvial landforms that have been identified on the surface of Mars [e.g., Dickson and Head, 2009; Carr and Head, 2010], and the regular occurrence of temperatures below and above the freezing point of water, suggests that freeze-thaw weathering may have also occurred on Mars. Furthermore, the permafrost environment on Mars should promote weathering through ice segregation in near-surface permafrost, which is controlled by the suction the ice exerts on water [Murton *et al.*, 2006]. Rocks altered by one or more of these processes have been identified on the Martian surface by multiple Martian Rovers [e.g., Thomas *et al.*, 2005; Jagoutz, 2006; Eppes *et al.*, 2015].

The fracture of bedrock by weathering is fundamental to debris production and therefore to landscape development [e.g., Murton *et al.*, 2006]. Weathering is a complex interplay of dozens of various physical, chemical, and sometimes biological processes that occur at different spatial and temporal scales [Viles, 2001, 2013]. The resulting rate of weathering is essentially nonlinear and reacts strongly not only to environmental controls but also to the preconditioning of the rock mass, which itself has a long memory of, for example, prior stress from tectonic fields or stress events (e.g., impacts) [Hall *et al.*, 2012; Krautblatter and Moore, 2015]. Quantifying bedrock weathering rates on Mars can thus provide insights into past environmental and climatic conditions and might provide constraints on the rates of landscape development. Moreover, understanding the history of weathering rates on Mars may be a key source of information for the impact of extreme environmental changes on bedrock weathering rates beyond those experienced in the recent past on planet Earth.

On Earth, bedrock weathering rates are often defined and quantified as a backweathering rate (i.e., rockwall retreat rate) [e.g., Rapp, 1960; Söderman, 1980; Hinchliffe and Ballantyne, 1999; Sass, 2007; Krautblatter and Dikau, 2007; Moore *et al.*, 2009; Siewert *et al.*, 2012]. These rates are generally quantified by direct or indirect measurements of sediment loss from rock faces or alcoves and the associated sediment input to depositional slopes or aprons [e.g., Rapp, 1960; Hinchliffe and Ballantyne, 1999; Krautblatter and Dikau, 2007]. The widespread presence of alcoves on the walls of pristine impact craters on Mars thus enables quantification of recent backweathering rates. Note that in crater alcoves backweathering or rockwall retreat is not strictly controlled by weathering only, as part of the retreat might be related to erosion by geomorphic flows (backweathering is used analogous to backwearing).

Backweathering is the sum of rock falls and rock slope failures that cover magnitudes from 10^{-6} to 10^{10} m³ on Earth [Krautblatter and Moore, 2015]. These processes can be classified into debris falls, <10 m³; boulder falls, 10^{-10^2} m³; block falls, $10^2 - 10^4$ m³; cliff falls, $10^4 - 10^6$ m³; and rock avalanches > 10^6 m³ [e.g., Whalley, 1974; Krautblatter *et al.*, 2012]. Low-magnitude rock fall processes generally occur more frequently than high-magnitude processes, but the relative effectiveness of these processes varies between sites depending on the local conditions [Krautblatter *et al.*, 2012]. Local geological conditions that strongly influence backweathering rates include (1) lithology, (2) strength of the rock, (3) state of weathering of the rock, and (4) joint density, orientation, width, and continuity and infill [e.g., Selby, 1980; Krautblatter and Dikau, 2007].

Table 1. Study Crater Characteristics

Crater	Latitude	Longitude	Diameter (km)	Highest elevation (m)	Lowest Elevation (m)	Age (Ma)
Crater A	50.19°N	184.51°E	1.8	−3924	−4398	0.3 (0.15–0.8) ^a
Crater B	21.59°N	184.3°E	13.8	−2950	−4540	39 (30–60) ^a
Corinto	16.95°N	141.70°E	13.9	260	−1040	(0.1–3.0) ^b
Crater C	16.41°N	209.7°E	2.5	−3660	−4300	5.3 (4–8) ^a
Zunil	7.78°N	166.34°E	10.0	−2330	−3510	(0.1–1) ^c
Gratteri	17.72°S	199.90°E	6.9	570	−460	(0.7–2.0) ^c
Zumba	28.65°S	226.90°E	2.8	2350	1710	(0.1–0.8) ^{cd}
Gasa	35.72°S	129.45°E	6.5	580	−700	1.25 (0.6–2.4) ^e
Galap	37.66°S	192.93°E	5.6	1080	100	6.5 (5–9) ^a
Istok	45.11°S	274.2°E	4.7	2670	1840	0.19 (0.1–1.0) ^f

^aThis study (Figure 4).

^bFrom Golombek et al. [2014a].

^cFrom Hartmann et al. [2010].

^dFrom Schon et al. [2012].

^eFrom Schon et al. [2009].

^fFrom Johnsson et al. [2014].

Moore et al., 2009; Krautblatter and Moore, 2015]. Many of these factors are interconnected, and weathering is indirectly included in many of these parameters, e.g., the loss of rock strength and opening of joints are largely weathering phenomena. Lastly, the presence of liquid water greatly enhances weathering and thereby backweathering rates [e.g., Selby, 1980; Sass, 2005; Viles, 2013; Warke, 2013].

We hypothesize that backweathering rates in the alcoves of pristine impact craters are relatively high. Crater rims are generally oversteepened shortly after formation and consist of highly faulted, fractured, and fragmented materials [e.g., Kumar and Kring, 2008; Kumar et al., 2010; Wang et al., 2013; Kenkmann et al., 2014]. As a result, they are particularly prone to weathering shortly after their formation. Positions of alcoves appear to be preconditioned by the distribution of radial fractures in the crater wall bedrock, as shown for Meteor crater (i.e., Barringer crater) (USA) and Xiuyan crater (China) [Kumar et al., 2010; Wang et al., 2013]. Accordingly, the occurrence of dense fractures on impact crater walls and evidence for erosion along these fractures are found on Mars Exploration Rover images [e.g., Squyres et al., 2009]. Moreover, the pattern of fracturing around many gully alcoves is indicative of landsliding, for instance, on the pole-facing gully alcoves of Gasa crater [Okubo et al., 2011].

Here we aim to (1) determine recent (Late Amazonian) backweathering rates on Mars, (2) understand local and regional variability in backweathering rates and its implications for gully formation, (3) unravel the balance between recent backweathering and erosion, and (4) reveal any systematic difference (if any) between Martian and terrestrial backweathering rates. We further aim to (5) introduce and provide evidence for a “paracratering” concept explaining enhanced recent rockwall retreat rates on crater walls following crater formation. The term paracratering is inspired by the use of paraglacial to refer to sites on Earth exposed to enhanced rates of geomorphic activity after the retreat of a glacier [e.g., Church and Ryder, 1972; Ballantyne, 2002a].

This paper is organized as follows. We first detail study sites and methods. Then we present the calculated backweathering rates in the studied craters and their temporal, local, and regional variation. We discuss the occurrence of a paracratering decrease of backweathering rates with time and compare Late Amazonian backweathering rates to erosion rates and to terrestrial backweathering rates. We end with a discussion of the potential role of liquid water in backweathering and its implications for gullies on Mars.

2. Methods

2.1. Study Site Selection

We quantify Late Amazonian Martian backweathering rates in the alcoves of 10 pristine craters (Table 1 and Figures 1 and 2). These craters are distributed over the northern and southern equatorial (30°N–30°S) and midlatitude regions (30°N–60°S). The study sites were selected using the following criteria:

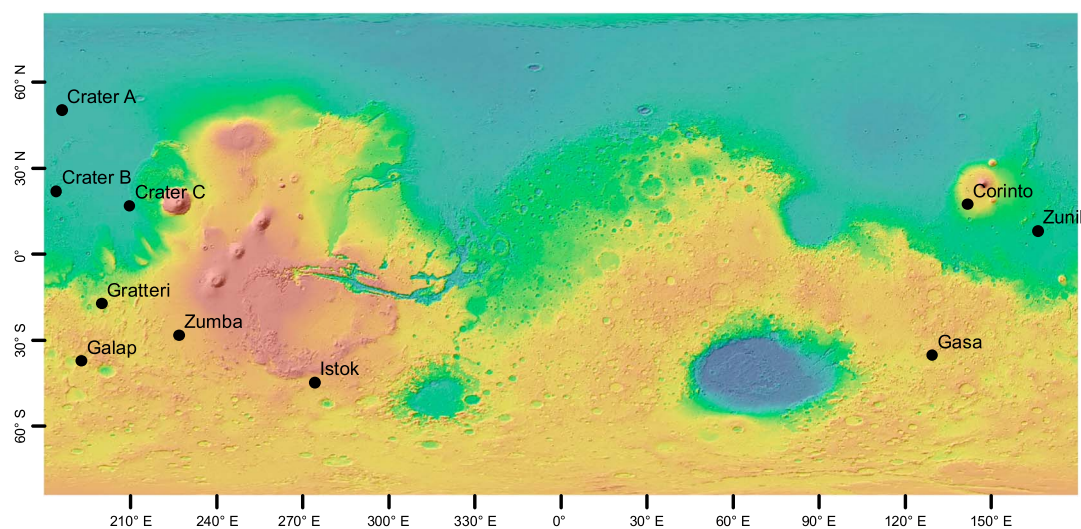


Figure 1. Study crater locations. Background topography is from the Mars Orbiter Laser Altimeter (red is high, blue is low elevation).

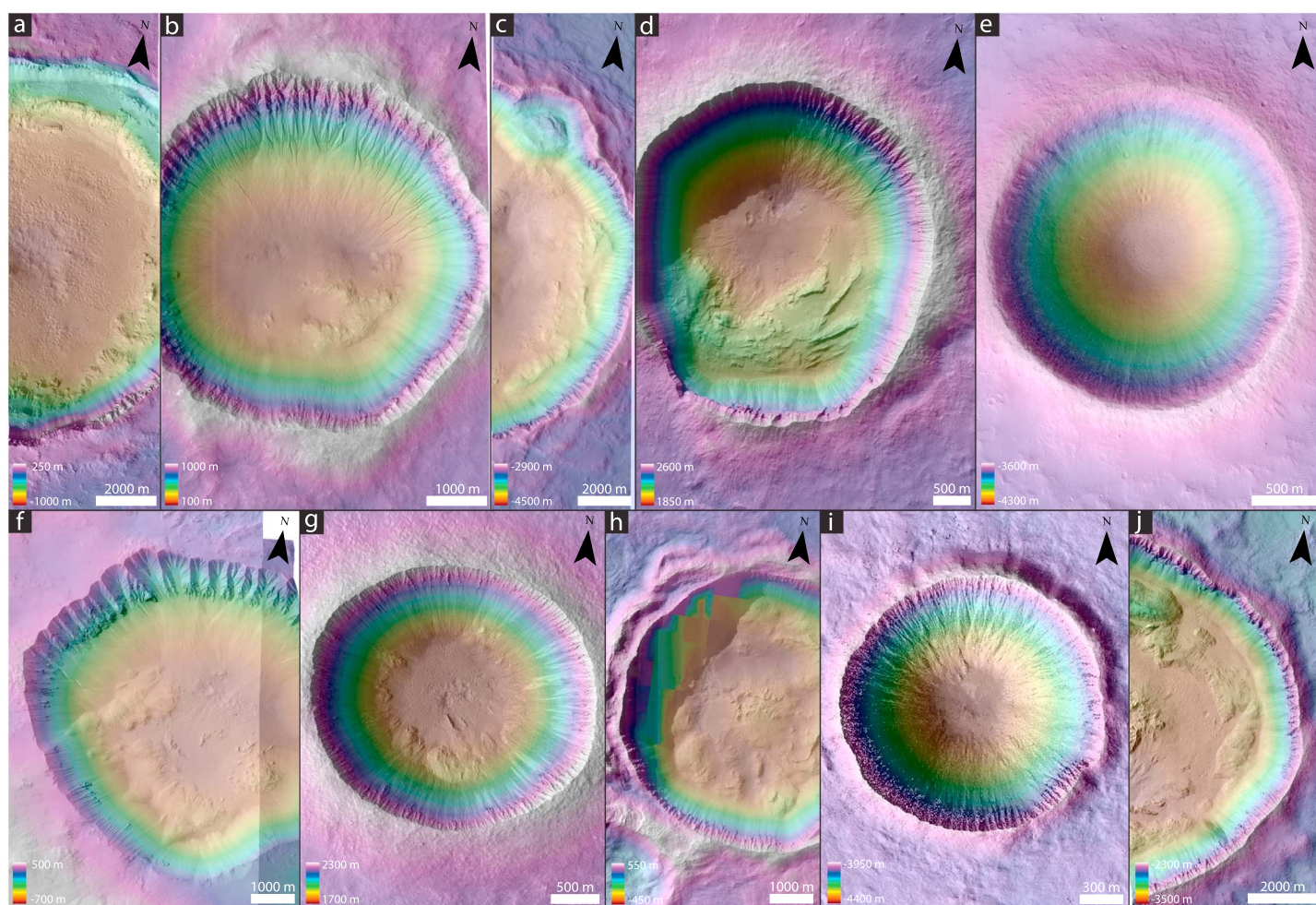


Figure 2. Image draped over colorized elevation model for the studied craters. Corresponding HiRISE image references and stereo pairs used to create the DEMs are found in Table 2. (a) Corinto crater (HiRISE image: PSP_003611_1970). (b) Galap crater (PSP_003939_1420). (c) Crater B (PSP_006774_2020). (d) Istok crater (PSP_006837_1345). (e) Crater C (PSP_005837_1965). (f) Gasa crater (ESP_014081_1440 and ESP_021584_1440). (g) Zumba crater (PSP_003608_1510). (h) Gratteri crater (PSP_010373_1620). (i) Crater A (ESP_025366_2305). (j) Zunil crater (PSP_002252_1880).

Table 2. List of Data Sources and Accuracy for the DEMs Used to Study Backweathering Rates

Crater	HiRISE Image 1	Pixel Scale	HiRISE Image 1	Pixel Scale	Convergence	Vertical Error	DEM Credit ^b
		Image 1 (m)		Image 2 (m)	Angle (deg)	(m) ^a	
Crater A	ESP_025498_2305	0.346	ESP_025366_2305	0.307	25.2	0.15	University of Arizona
Crater B	PSP_006774_2020	0.291	PSP_007341_2020	0.291	18.8	0.17	University of Arizona
Corinto	PSP_003611_1970	0.280	PSP_004244_1970	0.300	18.1	0.18	University of Arizona
Crater C	PSP_005837_1965	0.285	PSP_005837_1965	0.319	20.1	0.17	University of Arizona
Zunil	PSP_001764_1880	0.281	PSP_002252_1880	0.294	32.4	0.09	Open University
Gratteri	PSP_006800_1620	0.261	PSP_010373_1620	0.272	16.9	0.18	Open University
Zumba	PSP_002118_1510	0.255	PSP_003608_1510	0.278	18.1	0.17	University of Arizona
Gasa (1)	ESP_021584_1440	0.255	ESP_022217_1440	0.279	20.8	0.15	University of Arizona
Gasa (2)	ESP_014081_1440	0.507	ESP_014147_1440	0.538	20.7	0.28	University of Arizona
Galap	PSP_003939_1420	0.256	PSP_003939_1420	0.291	21.7	0.15	Open University
Istok	PSP_006837_1345	0.250	PSP_007127_1345	0.258	20.1	0.14	Open University

^aVertical precision was estimated via the method of Kirk *et al.* [2008].

^bDEMs from the University of Arizona were downloaded from the HiRISE website (<http://www.uahirise.org/dtm/>).

(1) pristine morphology; (2) Late Amazonian age; and (3) free of latitude-dependent mantle deposits (LDM), a smooth, often meters-thick deposit though to consist of ice containing dust, deposited from the poles down to the midlatitudes (30°N and 30°S) during periods of high orbital obliquity [e.g., Mustard *et al.*, 2001]. We selected craters that had already been dated in previous studies and/or for which a digital elevation model (DEM) had already been made (Tables 1 and 2).

Pristine craters are important chronostratigraphic markers for recent exogenic processes acting on the Martian surface [e.g., Schon and Head, 2012; Johnsson *et al.*, 2014]. Constraining the timing of these impacts facilitates quantifying rates of the exogenic processes acting upon craters since their formation [e.g., De Haas *et al.*, 2013, 2015a]. Pristine, Late Amazonian aged, craters enable (1) the measurement of relatively recent, Late Amazonian, backweathering rates and (2) the determination of their age because they have well-defined rays and ejecta on which the size-frequency distribution of superposed craters can be estimated.

Martian alcoves may incise into either bedrock, into the LDM, or into a combination of both [e.g., Aston *et al.*, 2011]. Alcoves that partly to completely incise into LDM can be eroded by melting of the ice incorporated in the LDM [Conway and Balme, 2014]. Therefore, only craters that mainly cut into original crater wall material or bedrock are used to determine backweathering rates. All selected craters are largely free of LDM deposits (see section 3.1).

2.2. Quantification of Backweathering Rates

On Earth, two different approaches exist to measure backweathering or rockwall retreat rates: direct and indirect measurements [Krautblatter and Dikau, 2007]. Direct measurement approaches use sediment traps or repeat elevation models to calculate recent short-term sediment supply from a rockwall [e.g., André, 1997; Hungr *et al.*, 1999]. Indirect measurements estimate the volume of sediment release and/or storage to calculate the long-term rockwall retreat rates over the accumulation time span [Hinchliffe and Ballantyne, 1999; Sass, 2007; Siewert *et al.*, 2012]. For Mars, we can only apply indirect measurements. A major source of uncertainty in indirect measurements is the estimation of sediment volume in depositional slopes or aprons, mainly because of the often unknown accumulation thickness and topography below the deposits [Siewert *et al.*, 2012]. On Earth, accumulation thickness is generally determined from incisions or sometimes drilling [e.g., Hinchliffe and Ballantyne, 1999] or geophysically using ground-penetrating radar [e.g., Siewert *et al.*, 2012]. On Mars, such analyses are not feasible.

This problem can be avoided by quantifying sediment loss volumes from alcoves rather than from depositional aprons. This is possible because alcoves generally develop on Martian crater walls, rather than uniform bedrock faces. Moreover, the volume loss in alcoves roughly equals the accumulated volume in depositional aprons in gully systems that mainly comprise bedrock [Conway and Balme, 2014].

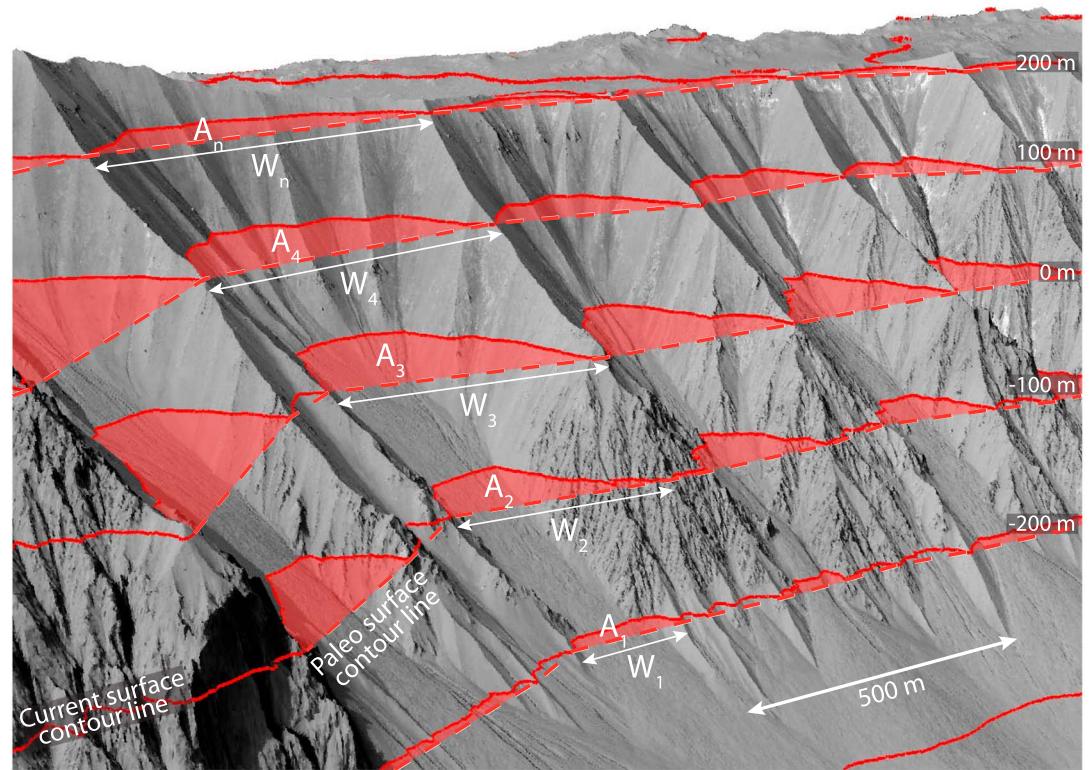


Figure 3. Method used for the derivation of backweathering rates from alcoves. Backweathering is defined as the spatially averaged retreat, inferred from the planimetric difference between the present-day and paleosurface contour lines. For the calculations, contour lines are derived from 1 to n , with a 1 m elevation interval. Background image shows Gasa crater gully alcoves (HiRISE image ESP_021584_1440).

We extract backweathering rate R in (mm yr^{-1}) from the spatially averaged retreat R_{sa} (mm), which is derived from the difference between the contour lines of the present-day topography and the inferred paleotopography, which we assume to be a straight line connecting the two sides of the alcove [Conway and Balme, 2014] (Figure 3):

$$R = \frac{R_{sa}}{T} \quad (1)$$

where T is the total time of exposure to weathering and erosion (year), assumed equal to the crater age. The spatially averaged retreat R_{sa} (mm) was inferred from the spatially averaged planimetric area A between the contour lines of the present-day topography and the paleotopography:

$$R_{sa} = \sum_{k=1}^n \frac{A_k/W_k}{n} \quad (2)$$

where W is the width of the planimetric area measured between the alcove crests on both sides of the catchment. Herein n is the total number of contour lines (contour lines were derived with 1 m elevation intervals for our calculations). Contour lines were determined from ~ 1 m/px DEMs derived from stereo images acquired by the High Resolution Science Imaging Experiment (HiRISE).

2.3. DEM Generation

When available, we used DEMs from the public HiRISE website (Table 2), otherwise we produced the DEMs using the software packages ISIS3 and SocetSet following the workflow of Kirk *et al.* [2008]. Vertical precision was estimated via the method of Kirk *et al.* [2008] where the vertical error equals maximum resolution/5/tan(convergence angle). These errors range from 0.09 m to 0.18 m, which are much smaller than the typical depth of the alcoves and therefore negligible.

Table 3. Comparison Between Backweathering Rates From Longyeardalen (Svalbard) Obtained From Talus Accumulation Thickness [Siewert *et al.*, 2012] and the Alcove Method Designed and Employed in This Study, Using a 25% Measurement Uncertainty on Top of the Age Uncertainty Following Siewert *et al.* [2012]^a

Site	Backweathering Rate (Siewert <i>et al.</i> [2012]) (mm yr ⁻¹)	Backweathering Rate (Alcove Method) (mm yr ⁻¹)
SE facing slope, site 1	0.52 (0.33–0.96)	1.49 (1.06–1.95)
NW facing slope, site 1	1.04 (0.60–1.72)	1.13 (0.80–1.48)
NW facing slope, site 2	1.17 (1.08–1.96)	1.07 (0.77–1.41)
NW facing slope, site 3	0.86 (0.61–1.51)	0.36 (0.26–0.47)
Total range	0.90 (0.33–1.96)	1.01 (0.26–1.95)

^aSee Figure S1 and Data Set S1 for raw data.

2.4. Age Determination

For craters that were already dated in other studies we used the ages reported from literature (Table 1) [Schon *et al.*, 2009, 2012; Hartmann *et al.*, 2010; Johnsson *et al.*, 2014; Golombek *et al.*, 2014a]. The other craters were dated based on the size-frequency distribution of impact craters superposed on the ejecta blanket and/or rim of the craters using HiRISE images (Crater A) or images from the Mars Reconnaissance Orbiter Context Camera (CTX) (Crater B, Crater C, and Galap crater). Superposed craters were identified by their bowl-shaped form. We defined crater ages based on the crater-size-frequency distribution using the chronology model of Hartmann and Neukum [2001] and the production function of Ivanov [2001]. Crater counts were performed using Crater Tools 2.1 [Kneissl *et al.*, 2011], and crater-size-frequency statistics were analyzed with Crater Stats 2 [Michael and Neukum, 2010]. The uncertainty in crater age can be relatively large; the minimum and maximum age typically differ by a factor of 2 to 10 (Table 1).

2.5. Uncertainties

Inferred backweathering rates from alcoves are subject to multiple measurement uncertainties. In a closed system, the volume of material eroded from the alcoves is similar to the volume of material deposited in the associated depositional apron, when corrected for deposit porosity. Alcove crests will probably be partly weathered and a portion of the weathered material is often temporally stored on the alcove floor, resulting in a slight underestimation of backweathering, and small geometrical errors may arise from digitizing alcove crests. Extracting a representative backweathering value from all backweathering contours per catchment results in a relatively small error; the median and average value are typically similar within 10%, and maximum values are typically 2–4 times the median value.

Errors of similar magnitude are associated to backweathering rates inferred from depositional aprons, as often applied on Earth, resulting from uncertainties in the talus thickness, talus porosity, and depositional apron delineation [e.g., Hinchliffe and Ballantyne, 1999; Siewert *et al.*, 2012]. The estimated rockwall area is also a source of uncertainty as it is a fractal property, and area will increase with decreasing measuring scale [Hoffmann and Schrott, 2002]. Moreover, the rockwall can be buried over time because of increasing amounts of accumulated scree in the talus cone, decreasing the height of the exposed rockwall. Siewert *et al.* [2012] estimate the total error to be 25%, excluding errors associated to dating of the accumulated time of backweathering. Further, it is often unknown whether backweathering rates are constant over time [McCarroll *et al.*, 2001; Ballantyne and Stone, 2013] or whether covered (e.g., moraine) deposits sometimes lead to an overestimation of accumulated talus volumes [Sass and Krautblatter, 2007].

To validate our approach, we compare Holocene backweathering rates from Longyeardalen (Svalbard) inferred from the accumulation thickness of four talus cones [Siewert *et al.*, 2012] with the rates calculated from the associated alcoves using the methods employed here. For this analysis, we use an airborne High-Resolution Stereo Camera (HRSC-AX) DEM, with a spatial resolution of 0.5 m that we upscaled to a 1 m spatial resolution, similar to the spatial resolution of the HiRISE DEMs used (Figure S1 in the supporting information) (see Hauber *et al.* [2011] and De Haas *et al.* [2015b] for a detailed description of the HRSC-AX DEM). The Holocene backweathering rates in Longyeardalen inferred from talus cone accumulation range from 0.33 to 1.96 mm yr⁻¹ [Siewert *et al.*, 2012]. These rates compare very well to the backweathering rates inferred from the alcoves, which range from 0.26 to 1.95 mm yr⁻¹ (Table 3). The values inferred from both methods are very

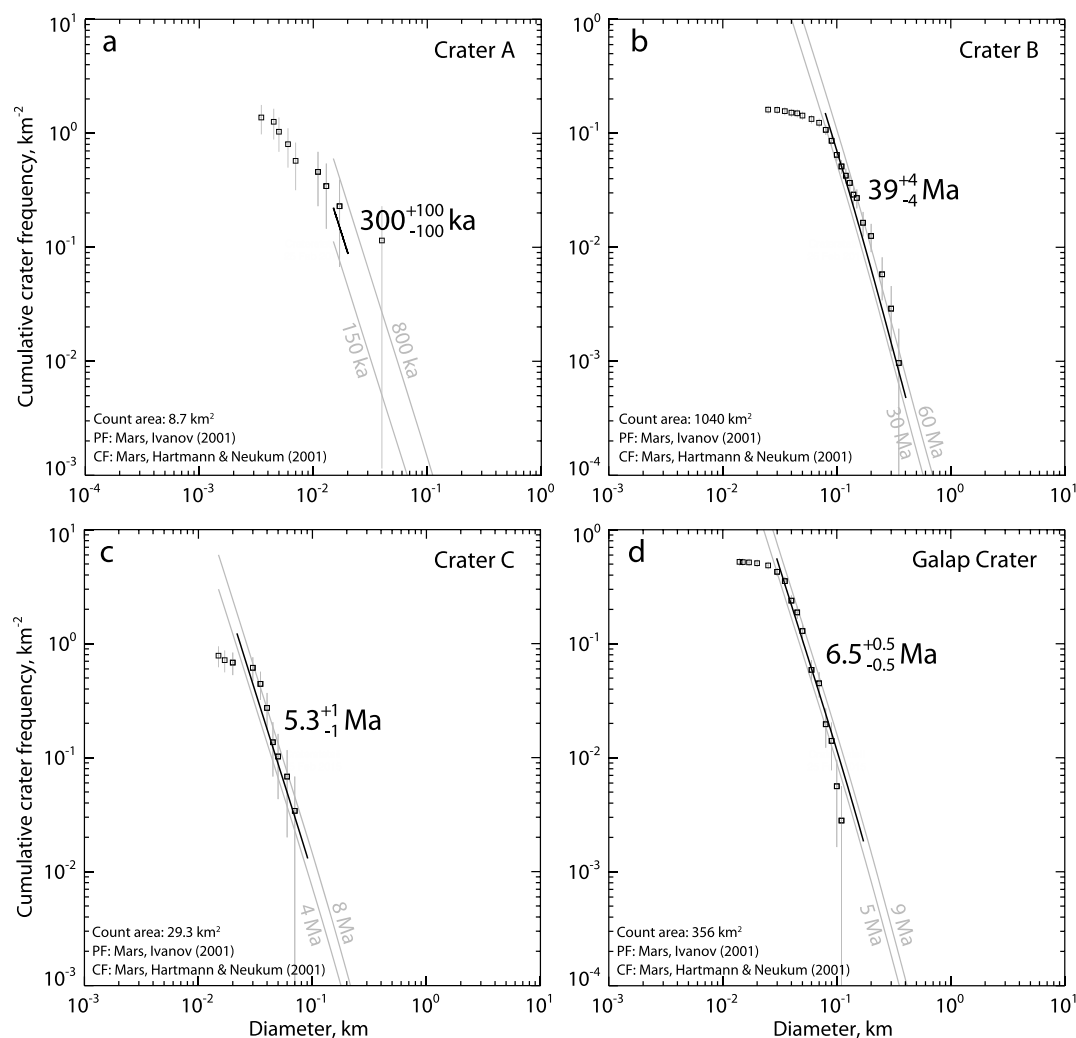


Figure 4. Crater-size-frequency distributions of dated craters. (a) Crater A. The size-frequency distribution indicates an absolute model age between 150 and 800 ka. The best fit absolute model age is $\sim 300 \pm 100$ ka. Count performed on HiRISE image ESP_025366_2305. (b) Crater B. The size-frequency distribution indicates an absolute model age between 30 and 60 Ma. The best fit absolute model age is $\sim 39 \pm 4$ Ma. Count performed on CTX images P16_007341_2013_XN_21N175W and B17_016360_2017_XN_21N175W. (c) Crater C. The size-frequency distribution indicates an absolute model age between 4 and 8 Ma. The best fit absolute model age is $\sim 5.3 \pm 1$ Ma. Count performed on CTX image P12_005837_1966_XI_16N150W. (d) Galap crater. The size-frequency distribution indicates an absolute model age between 5 and 9 Ma. The best fit absolute model age is $\sim 6.5 \pm 0.5$ Ma. Count performed on CTX image B07_012259_1421_XI_37S167W.

similar on sites 1 and 2 on the NW facing slope. For site 3 on the NW facing slope, the backweathering rate inferred from the alcove is approximately 2.5 times lower than the rate inferred from the talus cone, whereas for the site on the SE facing slope the backweathering rate inferred from the alcove is approximately 3 times larger than the rate inferred from the talus cones. As both methods are subject to potential errors, we assume that backweathering rates inferred from alcoves are accurate within factors 2–3 but are generally more accurate.

The uncertainty range on backweathering rates that results from crater age uncertainties (factors 2 to 10) is thus larger than the uncertainty that results from determining total backweathering in the alcoves. However, the variability of backweathering rates of the alcoves within craters ranges from 1 to 3 orders of magnitude and is therefore larger than the uncertainties associated with the methods employed to calculate backweathering rates. Therefore, we neglect the latter for simplicity and use the 25th and 75th percentile-sized alcoves per crater to indicate the backweathering range per crater in the figures throughout this article.

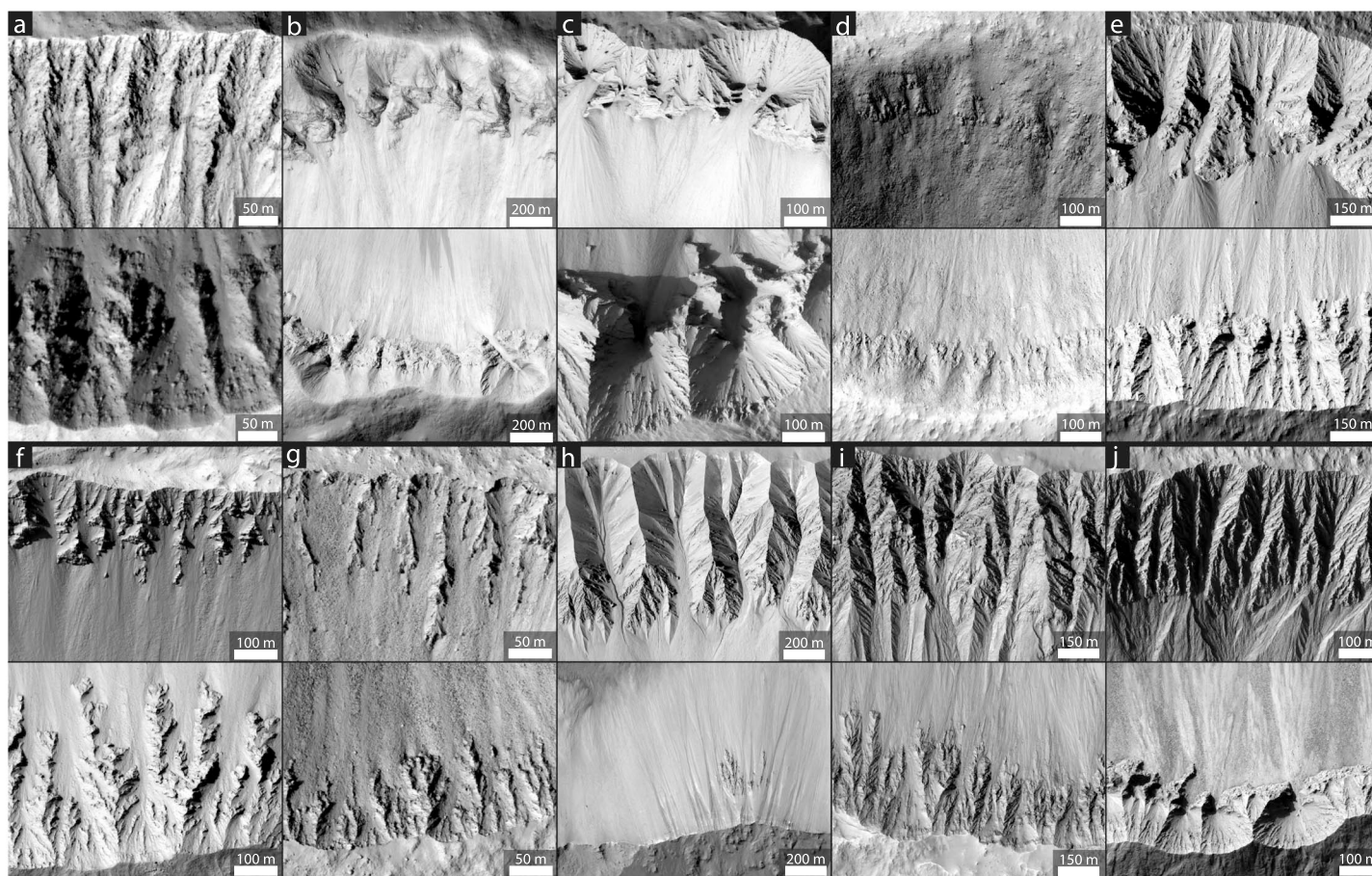


Figure 5. Alcove morphology. For each crater, a portion of the northern wall is displayed on the top panels, and a portion of the southern wall is displayed on the bottom panels. North is up in all images. (a–e) Northern latitude craters for which the southern wall is pole facing. (f–j) Southern latitude craters for which the northern wall is pole facing. Crater A (HiRISE image: ESP_025366_2305; Figure 5a). Crater B (PSP_007341_2020; Figure 5b). Corinto crater (PSP_004244_1970; Figure 5c). Crater C (PSP_005837_1965; Figure 5d). Zunil crater (PSP_002252_1880; Figure 5e). Gratteri crater (PSP_006800_1620; Figure 5f). Zumba crater (PSP_003608_1510; Figure 5g). Gasa crater (ESP_021584_1440; Figure 5h). Galap crater (PSP_003939_1420; Figure 5i). Istok crater (PSP_006837_1345; Figure 5j).

3. Results

3.1. Crater Age, Geology, and Lithology

The studied craters range in diameter from 1.8 to 13.9 km (Table 1). They are located at various altitudes, ranging from Istok crater with a highest point of 2670 m, down to Crater B for which the lowest part of the crater floor is located at -4540 m. The studied craters range in age from ~ 0.19 to ~ 39 Ma (Table 1 and Figure 4), but all craters except for Crater B are younger than 6.5 Ma.

The craters formed in various terrains, ranging in age from Noachian to Late Amazonian (Table 1). Craters A, B, and C, Corinto crater, Zunil crater, and Zumba crater all formed in volcanic terrains [Tanaka *et al.*, 2014]. Gratteri, Gasa, Galap, and Istok formed in Noachian terrain of undifferentiated origin on the geological map of Tanaka *et al.* [2014]. However, in the vicinity of these craters, there is no evidence for any type of sedimentary deposit (i.e., large channels), suggesting a volcanic origin. The lithology of the studied alcoves, therefore, probably predominantly consists of volcanic rocks, most likely basalt, which is the most common rock type on Mars [Bandfield *et al.*, 2000]. One notable exception might be Gasa crater, which is located within an older impact crater. Impact melt and impact breccia might therefore be the dominant bedrock lithology in Gasa crater [Okubo *et al.*, 2011]. Note that although the original bedrock material is probably volcanic in origin, crater walls are likely partly covered by allogenic and fall-back breccias, such as observed on Meteor crater on Earth [Kumar *et al.*, 2010]. Moreover, the rims of impact craters generally consist of highly faulted, fractured, and fragmented materials [e.g., Kumar and Kring, 2008; Kenkmann *et al.*, 2014].

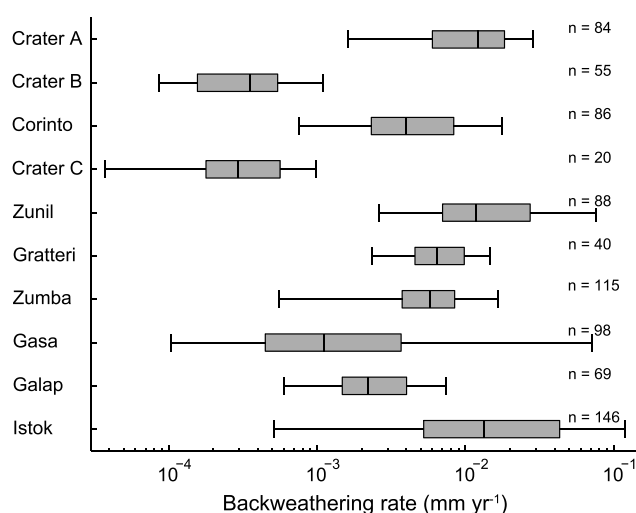


Figure 6. The distribution of backweathering rates found for the alcoves in each of the studied craters. The best fit crater age is used to convert total backweathering into a backweathering rate. Boxes indicate quartiles, the line crossing the boxes indicates the median, and whiskers indicate the 5th and 95th percentile backweathering rates. Number of measured alcoves per crater is denoted by n . See Figures S2–S11 and Data Set S1 for raw data.

3.2. Alcove Morphology

3.2.1. Equatorial Craters

The alcoves of the studied equatorial craters (between 30°N and 30°S) range from poorly developed to well-developed alcoves with sharply defined edges (Figure 5). Crater C exposes very shallow, poorly developed, alcoves on parts of its northwestern and southeastern walls (Figure 5d), whereas alcoves are absent on the rest of the crater wall. Shallow and narrow alcoves with poorly developed debris chutes are cut into the crater rim of Zumba crater (Figure 5g). Although these alcoves are larger than those found in the walls of Crater C, they are less well developed than those in the other equatorial craters. The alcoves in these remaining equatorial craters (Crater B, Corinto, Gratteri, and Zunil craters) (Figures 5b, 5c, 5e, and 5f) are larger and

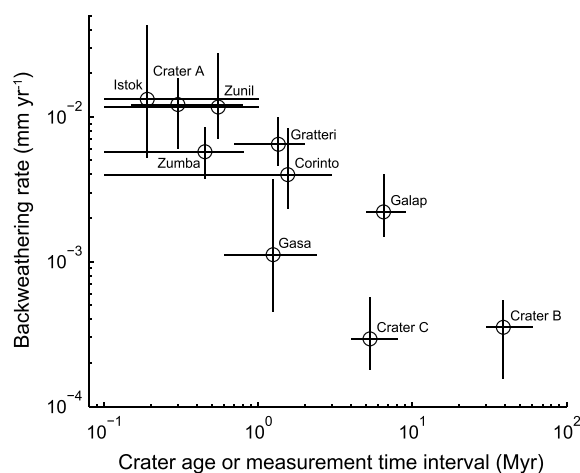


Figure 7. Median backweathering rate per crater as a function of crater age (= measurement time interval). Median backweathering rates decrease with increasing crater age. The circles are the best fit crater ages and the median backweathering rates per crater. Error bars denote estimated minimum and maximum crater age and the 25th and 75th percentile backweathering rates per crater.

The studied craters are largely free of LDM deposits. The LDM was not deposited below 30°N and 30°S [e.g., Mustard et al., 2001; Head et al., 2003], so the equatorial craters are free of LDM, which is supported by a visual inspection. Of the selected midlatitude craters, Gasa (and also Zumba, which is here defined as an equatorial crater) postdate the latest LDM mantling episode [Schon et al., 2012]. Moreover, Istok and Galap craters are presumably free of LDM deposits [Johnsson et al., 2014; De Haas et al., 2015a, 2015c], which is testified by the presence of highly brecciated alcoves hosting many boulders that solely expose bedrock and the absence of landforms associated with the LDM, such as moraine-like ridges and polygonally patterned ground. Crater A has similar characteristics, and therefore probably also postdates the latest LDM mantling episode.

have sharp, well-defined edges. Moreover, the alcoves of these craters and those of Zumba crater are generally roughly similar in planform shape and morphometry on all slope orientations, although the equator facing slopes are generally slightly larger.

All equatorial crater alcoves expose brecciated bedrock material and host meter-sized boulders. The alcoves are connected to steep depositional aprons, which can be defined as colluvial fans or talus cones [e.g., Blikra and Nemec, 1998; De Haas et al., 2015b]. These aprons typically have depositional slopes near the angle of repose, relatively short radial lengths compared to gully aprons, a downslope coarsening texture, and topographically smooth surfaces. These characteristics suggest a formation by rockfalls and dry grain flows and/or rock avalanches, transporting material from the alcoves to the depositional fans in the absence of liquid water [e.g., Conway et al., 2011; De Haas et al., 2015c].

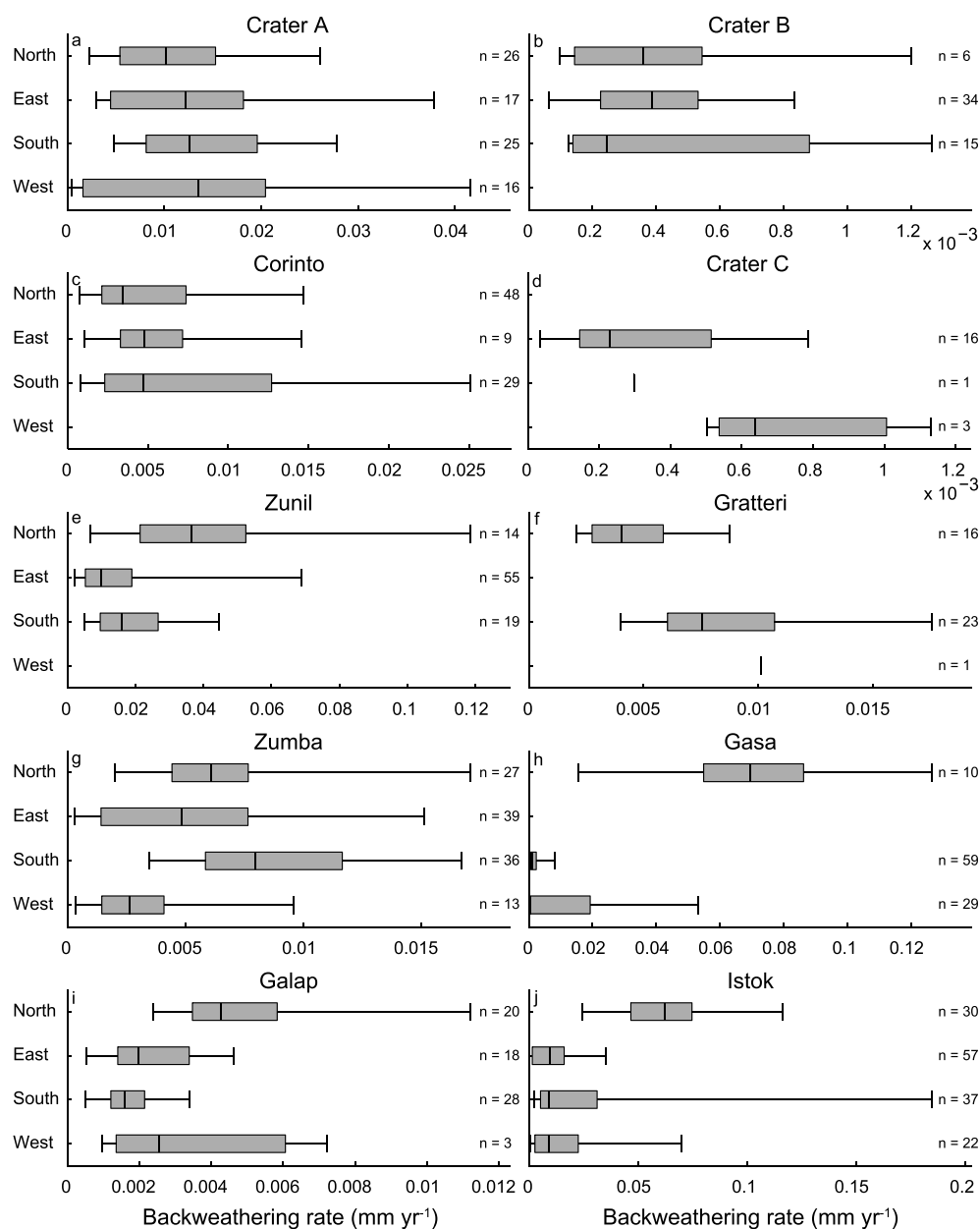


Figure 8. Backweathering rate distribution per orientation of the crater slope. Note that north represents the northern crater wall, which is south facing. (a) Crater A. (b) Crater B. (c) Corinto crater. (d) Crater C. (e) Zunil crater. (f) Gratteri crater. (g) Zumba crater. (h) Gasa crater. (i) Galap crater. (j) Istok crater. Crater A, Crater B, Corinto crater, Crater C, and Zunil crater are located on the Northern Hemisphere, while the other craters are located on the Southern Hemisphere. The best fit crater age is used to convert total backweathering into a backweathering rate. Boxes indicate quartiles, the line crossing the boxes indicates the median, and whiskers indicate the 5th and 95th percentile backweathering rates. Number of measured alcoves per crater is denoted by n .

3.2.2. Midlatitude Craters

The studied midlatitude craters ($>30^\circ\text{N}$ and $>30^\circ\text{S}$) differ from the equatorial craters by the presence of gullies on the pole-facing slopes of Gasa, Galap, and Istok craters. In Gasa, Galap, and Istok craters the largest alcoves are located in the middle of the northern, pole-facing, rim, and the alcoves become progressively smaller in clockwise and counterclockwise directions. The largest alcoves have a crenulated shape and are generally complex, consisting of multiple subalcoves (Figures 5h–5j). The sharp divides between the alcoves and the upper rims often expose fractured bedrock material, which appears to be highly brecciated and contains many boulders. The alcoves are connected to large gully fans, whose stratigraphy and morphometry

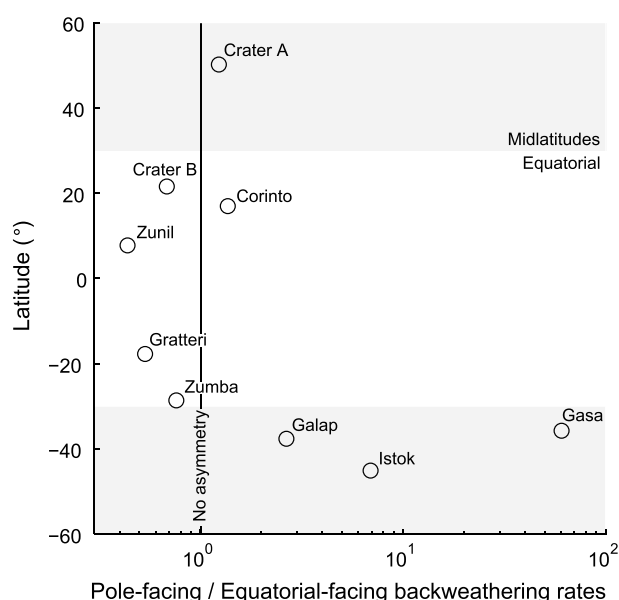


Figure 9. The ratio of pole-facing to equatorial-facing median backweathering rate per crater as a function of latitude. Larger alcoves and higher backweathering rates are present on the pole-facing, gullied, slopes of the studied midlatitude craters compared to the slopes on the other side of the crater. The opposite is true for the totally ungullied equatorial slopes except for Corinto crater.

suggest formation by aqueous flows [Conway *et al.*, 2011; Schon *et al.*, 2012; Schon and Head, 2012; Johnsson *et al.*, 2014; De Haas *et al.*, 2015a, 2015c]. The nonpole-facing, eastern, southern, and western walls of these craters are characterized by poorly developed, narrower and shallower, alcoves. These alcoves are similar in morphology and morphometry to the alcoves of the studied craters in the equatorial regions. Similar to the equatorial examples, they are also connected to steep talus cones suggesting a dry formation.

Crater A is a notable exception. The crater has relatively well-defined and roughly similar-sized alcoves on all azimuths (Figure 5a). These alcoves are similar to those of the nongullied slopes of the other midlatitude craters. On the north and NW slopes of the crater, channels are present in the talus slopes, suggesting the potential presence of liquid water in formation of the alcoves and aprons. We estimate, however, that these systems

predominately formed by dry processes as the bulk of the talus deposits have a morphometry, morphology, and texture indicative of dry rockfall and grain flow processes [De Haas *et al.*, 2015c].

3.2.3. Local and Regional Variations

Backweathering rates and their variability can change significantly on slopes with different orientations within craters (Figure 8). The backweathering rates on the northern slopes of Gasa, Galap, and Istok craters are much larger than those on the slopes with other azimuths (Figures 8h, 8i, and 8j). This agrees well with the large gully alcoves that are present on the northern slopes of these craters (Figures 5h, 5i, and 5j). The variability of backweathering rate on slopes with different orientations is generally smaller on the equatorial craters.

3.3. Backweathering Rates

The backweathering rates inferred from the alcoves in the studied craters range between 10^{-4} and 10^{-1} mm yr⁻¹ (Figures 6 and S2–S11 and Data Set S1). Backweathering rates typically vary by 1 order of magnitude between different alcoves within the craters. However, the variation is much larger in midlatitude craters, up to 3 orders of magnitude for Gasa and Istok craters, mainly because of the presence of gullied slopes (see section 3.3.2). There are similarly large differences in backweathering rates between craters, varying up to 3 orders of magnitude. We found that these differences are mainly caused by differences in crater age.

3.3.1. Temporal Variations

The inferred backweathering rates are highly dependent on crater age, and thus measurement time interval (Figure 7). The backweathering rates decrease strongly with crater age, and measurement time interval explains the largest variability in backweathering rates between craters. Backweathering rates are $\sim 10^{-2}$ mm yr⁻¹ for craters younger than 1 Ma, whereas they decrease down to $\sim 10^{-3}$ mm yr⁻¹ for craters approximately 10 Myr old. When corrected for measurement time interval, the backweathering rates only vary up to 1 order of magnitude between craters.

Zumba crater, Gasa crater, and Crater C have been exposed to relatively low backweathering rates. This agrees well with the poorly developed alcoves that we observed in Zumba crater and Crater C (section 3.2). Gasa crater has very large gullied alcoves on its pole-facing slopes, whereas very small, poorly developed, alcoves are present on the slopes with nonpolar azimuths. The median backweathering rate in Gasa is therefore relatively low, while the large pole-facing alcoves have much higher rates that conform to the general trend (Figure 6).

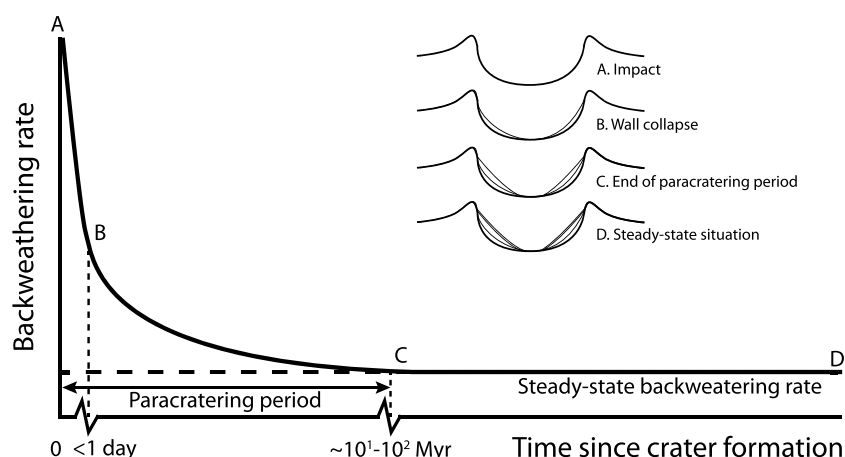


Figure 10. The temporal evolution of paracratering backweathering rates. Following crater formation the crater walls collapse, and pristine alcoves are rapidly formed (<1 day). Afterward, backweathering rates remain high for a prolonged period (at least $10^1 - 10^2$ Myr) but slowly decrease toward steady state backweathering rates. The paracratering period of enhanced backweathering rates starts after crater formation and ends when the backweathering rates have declined to the long-term steady state backweathering rate.

This latitude-dependent asymmetry can be summarized on a plot of latitude versus the asymmetry between pole-facing and equatorial-facing backweathering rates (Figure 9). The backweathering rates on the pole-facing slopes of the studied midlatitude craters are larger than those on the equator-facing slopes. This asymmetry is relatively large and can be up to a factor of ~ 60 (Gasa crater). In contrast, the studied craters in the equatorial regions have larger backweathering rates on the equator-facing slopes than on the pole-facing ones, except for Corinto crater. The asymmetry appears to increase toward the equator. This trend should, however, be interpreted with care since we only have five data points. Further study is required.

4. Discussion

Despite the observation that planet-wide weathering and erosion rates have dropped to very low values following the Noachian period [Bibring et al., 2006; Golombek et al., 2006; Carr and Head, 2010; Ehlmann et al., 2011], our results support recent observations of enhanced local weathering and erosion rates in the last few millions of years on Mars [e.g., De Haas et al., 2013; Golombek et al., 2014b].

The results also suggest that there is a paracratering decrease of backweathering rates over time. Additionally, the dependence of backweathering asymmetry on latitude (Figure 9) provides valuable insights into the weathering mechanisms acting on the crater alcoves and the role of liquid water therein, which has important implications for gully formation. Below we discuss these insights and implications. Furthermore, we discuss how our results compare to Late Amazonian erosion rates reported by others, as well as to terrestrial backweathering rates from Meteor crater and from various Holocene Arctic, Nordic, and Alpine rock faces.

4.1. Decreasing Backweathering Rates Over Time

The average Late Amazonian backweathering rates inferred from crater wall alcoves decrease with crater age (Figure 7). These declining backweathering rates can probably be mainly attributed to a paracratering decrease of backweathering rates over time (Figure 10).

Deglaciation exposes oversteepened rock slopes, which are often highly fractured due to enhanced stress relaxation caused by debuttrressing (removal of the support of adjacent glacier ice), resulting in enhanced backweathering rates that decline toward background rates over time [e.g., André, 1997; Hinchliffe and Ballantyne, 1999; Ballantyne, 2002a]. This is referred to as a paraglacial decrease in backweathering rates over time.

The interior parts of crater rims are generally oversteepened shortly after their formation and consist of highly faulted, fractured, and fragmented materials [Kumar and Kring, 2008; Kumar et al., 2010; Kenkmann et al., 2014], similar to recently deglaciated rockwalls. As a result, they are particularly prone to backweathering shortly after their formation. Many studies have shown that backweathering rates increase with increasing joint or

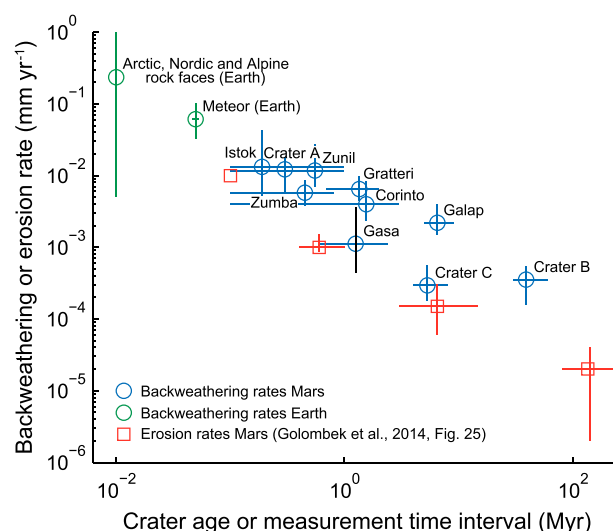


Figure 11. Median backweathering rates as a function of crater age (= measurement time interval) for the studied Martian craters, Meteor crater (i.e., Barringer crater) on Earth, the reported terrestrial rock faces given in Figure 12 and Table S1, and the erosion rates reported in Golombek et al. [2014b] (as shown in their Figure 25, compiled from data of Malin and Edgett [2000], McEwen et al. [2005], Golombek et al. [2006], De Haas et al. [2013], Golombek et al. [2014b], and Farley et al. [2014]). Backweathering rates for Meteor crater were derived with the method applied to the Martian craters, using a LiDAR DEM with 1 m spatial resolution (Figure S12 and Data Set S1; <http://www.lpi.usra.edu/publications/books/barringer/crater/guidebook/LiDAR/>), the age of Meteor crater is 49 ± 3 ka [Sutton, 1985; Nishiizumi et al., 1991; Phillips et al., 1991]. The circles and squares are the best fit crater ages and the median backweathering/erosion rates. Error bars denote estimated minimum and maximum crater age and the 25th and 75th percentile backweathering/erosion rates. For simplicity, the terrestrial rock face backweathering rates are given an age of 10 ka in the diagram (approximately the start of the Holocene).

fracture density [e.g., Selby, 1980; Douglas, 1980; Fahey and Lefebvre, 1988; André, 1997; Sass, 2005; Moore et al., 2009; Krautblatter and Moore, 2015]. More specifically, Sass [2005] showed empirically in the Northern and Central European Alps that backweathering on average increases linearly with joint density. The oversteepening of rock slopes increases the stress regime acting within a rock slope. This promotes rock slope failure at various scales, ranging from debris falls to large-scale catastrophic rock slope failures, along preexisting joint sets or other planes of weakness [e.g., Ballantyne, 2002a]. Following impact, crater walls are thus relatively unstable and backweathering rates are high. The most unstable parts of the crater wall will rapidly fail, after which a more stable rock slope configuration develops. For example, Kumar et al. [2010] suggest that parts of the backweathering in the alcoves of Meteor crater might have occurred almost immediately after the impact, and a response time of several thousand years following deglaciation is hypothesized for terrestrial rockwalls, reflecting the time needed for stress-related fracturing to yield a critical path for large-rock slope failures [Einstein et al., 1983; Prager et al., 2008]. The effects of fractures in promoting backweathering in crater walls are evident from alcoves in terrestrial impact craters that are often associated with the presence of radial

fractures [Kumar et al., 2010; Wang et al., 2013]. In short, backweathering rates in impact craters are initially high but decline to a slowly declining background rate or to a lower but rather constant background rate over time, as the crater wall becomes more stable. Such a decline can typically be described by an exhaustion model in which sediment yield decreases exponentially over time [Ballantyne, 2002b].

A major disadvantage of the paraglacial concept on Earth is that the interglacial timescale of 10^{-2} Myr of observations determined by Milankovitch cycles may be shorter than the relaxation time of rock slopes; possibly, we do not reach the steady state of rockfall activity in a single interglacial cycle in Alpine and Arctic valleys [Ballantyne and Stone, 2013; Viles, 2013; Krautblatter and Moore, 2015]. On Mars, we have the opportunity to observe the full exhaustion curve that only leads to a steady state after $10^1 - 10^2$ Myr, or possibly longer, suggesting that steady state rockfall activity is hardly reached in terrestrial rockwall systems.

Over long timescales, erosion, weathering, and sedimentation rates are dependent on measurement time interval ("Sadler effect" or timescale bias) [Sadler, 1981, 1999], because the rates of surficial geological processes are discontinuous and unsteady over time. They are variable in both magnitude and frequency in space and time and may incorporate heavy-tailed hiatuses that separate the actual weathering and erosion events. Moreover, higher magnitude events tend to occur with lower frequency [e.g., Gardner et al., 1987; Krautblatter et al., 2012], and rates of surficial processes can thus incorporate longer intervals of relatively low activity, producing an apparent slower rate [Gardner et al., 1987]. It is unknown over which timescales the decrease in backweathering rates is also significantly influenced by a timescale bias, but Golombek et al. [2014b] attribute

the decrease in small crater denudation rates over 0.1–100 Myr timescales mainly to topographic diffusion (see below). Accordingly, we hypothesize that the observed decrease in backweathering rates over time in the studied pristine craters can be predominantly attributed to paracratering effects rather than a timescale bias.

4.2. Late Amazonian Backweathering Versus Erosion Rates

Late Amazonian small crater modification rates, i.e., the denudation of the crater rim and infill of the crater depression, decrease with increasing measurement time interval on Meridiani Planum (Figure 11) [Golombek *et al.*, 2014b], similar to the observed decrease in backweathering rates over time. Golombek *et al.* [2014b] show that small crater denudation rates decrease from $\sim 10^{-3}$ mm yr $^{-1}$ for craters younger than 1 Ma to $< 10^{-4}$ mm yr $^{-1}$ for craters 10–20 Ma and $< 10^{-5}$ mm yr $^{-1}$ when averaged over ~ 100 Myr to 3 Gyr in the Amazonian and the Hesperian. Moreover, Golombek *et al.* [2014b] outline that similar erosion rates for similar measurement time intervals were found by Malin and Edgett [2000], McEwen *et al.* [2005], De Haas *et al.* [2013], and Farley *et al.* [2014] (Figure 11).

Golombek *et al.* [2014b] attribute the decreasing erosion rates over time to topographic diffusion. Topographic diffusion is also used to explain the rapid smoothing of Late Amazonian gully fan surfaces on Mars [De Haas *et al.*, 2013]. Immediately after impact, a crater rim is formed that is out of equilibrium with the eolian regime, which results in rapid erosion of the weak ejecta blocks and other rim deposits in the wind stream and deposition in quiet areas around these blocks and inside the craters [Golombek *et al.*, 2014b]. This is also a paracratering process, and it is in essence similar to the paracratering relaxation of backweathering rates when the crater wall progressively moves toward a more stable configuration.

The small crater modification rates observed by Golombek *et al.* [2014b] are approximately 1 order of magnitude lower than the backweathering rates we inferred from crater alcoves (Figure 11). The alcove backweathering rates are probably larger than the erosion rates because (1) crater walls are highly susceptible to backweathering and (2) crater erosion is more a “grain by grain” process, whereas backweathering spans grain by grain to large failures [e.g., Krautblatter *et al.*, 2012], which together result in a higher net rate. This explanation is supported by Okubo *et al.* [2011], who show that the pattern of fracturing around the crowns (upper parts) of the gully alcoves of Gasa crater is indicative of landsliding.

4.3. Martian Versus Terrestrial Backweathering Rates

Terrestrial rockwall retreat rates are highly variable in all environments and can vary up to 4 orders of magnitude (Figure 12) [e.g., Hinchliffe and Ballantyne, 1999; André, 2003; Glade, 2005; Krautblatter and Dikau, 2007; Siewert *et al.*, 2012]. The large variability mainly results from highly variable topography, lithology, and climatic conditions at different rock slopes [e.g., André, 1997]. Furthermore, part of the variability may be attributed to paraglacially enhanced backweathering rates on some rock slopes [e.g., Hinchliffe and Ballantyne, 1999; Ballantyne, 2002a], the wide range of direct and indirect methods employed [Krautblatter and Dikau, 2007], and the time span for which the backweathering rates are derived.

The inferred Martian backweathering rates are on average 1–2 orders of magnitudes below the range of reported Holocene terrestrial values (Figure 12). The highest Martian backweathering rates are similar to the lowest reported terrestrial Arctic, Nordic, and Alpine values. When corrected for time span, there is a remarkably good correspondence between the trend for Martian backweathering rates versus time interval and the terrestrial trend derived from Holocene backweathering rates and Meteor crater (Figure 11). Although it is not known how the Martian backweathering rates evolve toward relatively young ages (< 0.1 Ma), the remarkably good correspondence between backweathering rates on both planets suggests that they evolve similarly. Part of the correspondence between Martian backweathering rates in pristine craters to terrestrial rock faces might be attributed to the relatively high susceptibility of Martian crater walls to backweathering, balanced by the atmospheric conditions on Mars that are probably less favorable to weathering (e.g., restricted amounts of water) [e.g., Mischne *et al.*, 2003]. However, this does not explain the good correspondence between the backweathering rates in the Martian craters and Meteor crater, although this might be partly explained by the higher susceptibility to backweathering of the sedimentary bedrock wherein Meteor crater formed compared to the basaltic bedrock on Mars.

In contrast, Golombek *et al.* [2014b] show that Hesperian to Amazonian erosion rates are 3–4 orders of magnitude lower than typical terrestrial erosion rates when averaged over similar timescales, suggesting that, in general, Martian surface processes are dramatically slower than those on Earth. Golombek *et al.* [2014b] attribute this to the absence of liquid water as an important erosional agent on Mars. One explanation for

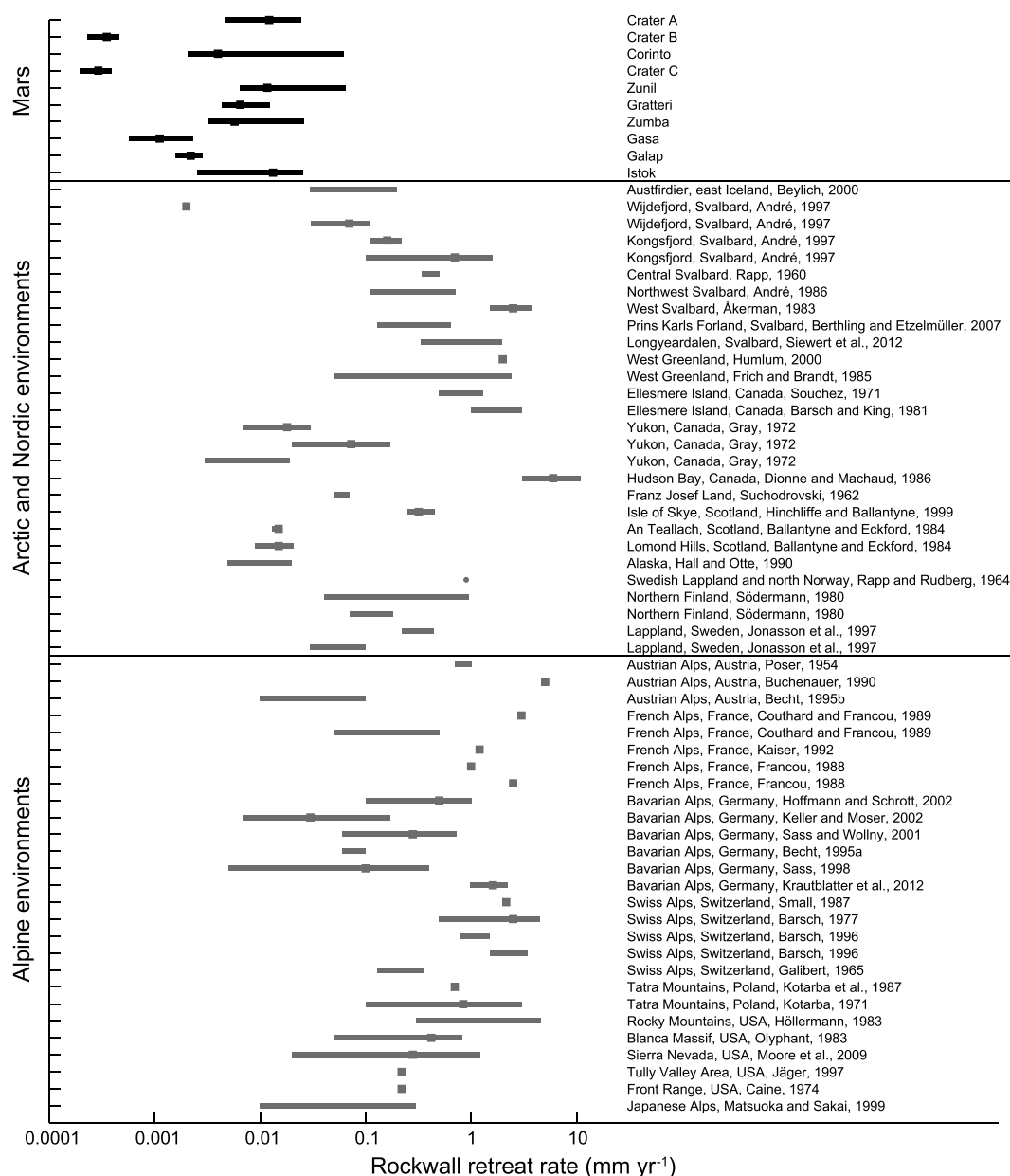


Figure 12. Comparison of the Martian rockwall retreat rates obtained in this study to terrestrial rockwall retreat rates from various Arctic, Nordic, and Alpine environments (extended from André [1997, 2003], Hinchliffe and Ballantyne [1999], and Glade [2005]). See Table S1 for raw data. Median backweathering rate per crater is used for the Martian data. The black square indicates result for best fit age, uncertainty is based on minimum and maximum age.

this discrepancy might be that the occasional presence of liquid water could more effectively enhance weathering and erosion rates on steep crater walls compared to relatively low-gradient small crater rims, as steep landscapes have naturally faster erosion rates than lower sloping landscapes [e.g., DiBiase et al., 2012].

4.4. The Potential Role of Liquid Water in Backweathering and Implications for Gullies

4.4.1. Liquid Water as Catalyst for Backweathering?

The backweathering rates in the pole-facing alcoves of the studied midlatitude craters are much larger than those on slopes with other azimuths, in contrast to the equatorial craters where the backweathering rates are more similar around the crater wall (Figures 8 and 9). The large pole-facing alcoves of Gasa, Galap, and Istok crater contain gullies, whereas gullies are absent on the crater slopes with nonpolar azimuths. These observations suggest that the enhanced backweathering rates in gullies are associated to the processes

leading to gully formation. Gullies have been hypothesized to have formed by aqueous debris flows and/or fluvial flows [e.g., Costard *et al.*, 2002; Dickson *et al.*, 2007; Conway *et al.*, 2011; Johnsson *et al.*, 2014; De Haas *et al.*, 2015c] or by water-free sediment flows, often associated with CO₂ ice sublimation [e.g., Treiman, 2003; Pelletier *et al.*, 2008; Dundas *et al.*, 2010; Cedillo-Flores *et al.*, 2011; Dundas *et al.*, 2014].

On the majority of nongullied areas on Mars, weathering induced by thermal cycling is probably the most important weathering mechanism on Mars [e.g., Viles *et al.*, 2010; Eppes *et al.*, 2015]. In contrast, the greatly enhanced backweathering rates in gully alcoves may result from the presence of liquid water, CO₂ ice, or both. The presence of liquid water generally results in enhanced weathering rates as shown on Earth [e.g., Selby, 1980; Sass, 2005; Krautblatter and Moser, 2009; Warke, 2013], by enhancing chemical modification rates, freeze-thaw cycles, and hydration-dehydration and crystallization cycles in the presence of salts, which are abundant on Mars [e.g., Clark and Hart, 1981; Rodriguez-Navarro, 1998; Jagoutz, 2006; Head *et al.*, 2011].

The effects of CO₂ ice accumulation and sublimation on fractured slopes under Martian conditions are currently unknown, because there are no terrestrial analogs of this process and no laboratory experiments on the effects of CO₂ on bedrock fracturing have been performed. If CO₂ ice has an effect on backweathering of fractured slopes, it would be very different from what is seen on Earth, as CO₂ cannot exist in its liquid form on Mars. Thus, freeze-thaw cycles and salt weathering would likely not be enhanced by the presence of CO₂. Furthermore, CO₂ ice deposits on Mars remain at or above the CO₂ condensation temperature. This is because when the surface temperature drops below the CO₂ condensation temperature, the atmosphere provides a continuous supply of CO₂; therefore, condensation is also continuous and prevents the ice cooling further. This is not the case for water ice, where the atmospheric supply runs out rapidly once the temperature drops below the condensation point and therefore the temperature in the ice can experience thermal cycles below zero, which probably causes most of the high latitude polygonally patterned terrains on Mars [Mangold, 2005]. This, for example, explains why the polygons seen on CO₂ slab ice are linked to brittle failure rather than to thermal contraction stresses [Portyankina *et al.*, 2012].

Based on these observations, the presence of liquid water is the most parsimonious accelerator of weathering rates on gullied crater slopes. This liquid water has probably been present during periods of high orbital obliquity [e.g., Williams *et al.*, 2009]. Nonetheless, CO₂ ice accumulation and sublimation cannot be fully ruled out as a catalyst for weathering in gully alcoves.

4.4.2. Gully Fan Formation and Modification

The high paracratering backweathering rates following crater formation (Figure 7) initially result in the presence of a lot of loose material that is available for transport in gully alcoves. This probably facilitates high sediment transport rates toward the gully fans and might explain the presence of large and well-developed gully fans in very young impact craters like Istok crater [Johnsson *et al.*, 2014; De Haas *et al.*, 2015a]. As backweathering rates decrease over time, the sediment supply rates decrease simultaneously and the gullies might transition from transport-limited to supply-limited systems [e.g., Glade, 2005]. Although this remains highly speculative, it might partly explain why gullies in very young impact craters are approximately the same size as those in much older impact craters. For example, the gully alcoves and gully fans in the relatively young Istok, Gasa, and Galap craters studied here (all younger than a few Ma) are fairly similar to those found in Hale crater as described by Reiss *et al.* [2011], which is a relatively old crater with an age of ~1 Ga [Jones *et al.*, 2011]. An alternative explanation might be that the gullies are subject to repeat erosional/deposition cycles driven by orbital cycles and the LDM [Dickson *et al.*, 2015], but this would not fully explain the small difference in alcove size between gullies with different ages. The majority of gullies studied by Dickson *et al.* [2015] are located within the LDM and are not systematically associated with bedrock alcoves. The mass balance of such gullies is dominated by the gain and loss of ice, which means the sediment transport is limited to the dust and other debris contained in the LDM [Conway and Balme, 2014]; therefore, they are isolated from the site of backweathering at the crater rim and cannot contribute to it. It is possible that, once it is established, the LDM forms a barrier to backweathering and once a certain threshold is reached it even inhibits gully formation entirely. New impacts clear away the LDM leaving the slope free to directly experience the full brunt of Mars atmospheric and hydrological cycles.

The high backweathering rates on the gullied midlatitude crater slopes, which can exceed those on the ungullied slopes in the same crater by more than 60 times (Figure 9), shows that weathering rates in gullies can be much higher than those in other areas on Mars. These enhanced weathering rates potentially explain why relatively young gully fan surfaces often host many meter-sized boulders and have notable relief, whereas these

features are typically absent on older gully fan surfaces [De Haas *et al.*, 2013, 2015c]. Moreover, this might also explain why boulder break down can occur within 1 Myr on gully fans [De Haas *et al.*, 2013], whereas boulders can be preserved for millions to billions of years on other Martian surfaces.

5. Conclusions

We derived recent, Late Amazonian, backweathering rates from the alcoves of 10 pristine equatorial and midlatitude impact craters on Mars. These backweathering rates range between 10^{-4} and 10^{-1} mm yr $^{-1}$ but decrease with increasing crater age. This paracratering decrease in backweathering rates over time mainly results from the oversteepened and highly fractured and faulted crater walls following impact, which makes the crater slopes highly susceptible to backweathering and results in initially high backweathering rates that decline over time as the crater wall stabilizes.

Late Amazonian backweathering rates are approximately 1 order of magnitude higher than Late Amazonian erosion rates. We attribute this to the high susceptibility to backweathering of crater walls and the fact that most erosional processes are a “grain by grain” process, while backweathering is the sum of grain by grain to large-scale slope failures. The Martian backweathering rates appear to be approximately similar to terrestrial rates inferred from Meteor crater and various Arctic, Nordic, and Alpine rock faces. Moreover, the long timescale before steady state backweathering rates are reached on Mars (at least 10^1 – 10^2) may suggest that steady state rockfall activity is hardly reached in terrestrial rockwall systems within interglacial timescales of 10^{-2} .

Backweathering rates have been much larger in the gullied pole-facing alcoves than in the ungullied, nonpole-facing slopes of the midlatitude craters. This is in contrast with the studied craters in the equatorial regions, where the rates are more similar around the crater wall and backweathering rates are generally even higher on the equator-facing slopes. We hypothesize that the higher backweathering rates in the gullied slopes of the midlatitude craters could be caused by liquid water acting as a catalyst for backweathering on these slopes but cannot yet evaluate the effect of processes related to CO $_2$ ice.

The paracratering decrease in backweathering rates over time might partly explain why gullies in very young impact craters are approximately the same size as those in much older impact craters. Additionally, once established the LDM might form a barrier to backweathering that retards or even inhibits gully formation.

Acknowledgments

Rockwall retreat data are attached as supporting information, the analyzed HiRISE images can be downloaded at the public HiRISE website (<https://hirise.lpl.arizona.edu/>). This work is part of the PhD research of T.d.H., supported by the Netherlands Organisation for Scientific Research (NWO) and the Netherlands Space Office (NSO) (grant ALW-GO-PL17-2012 to Maarten G. Kleinhans). S.J.C. is funded by a Leverhulme Trust grant RPG-397. We thank Teun van Buul for digitizing the alcoves of Corinto, Gasa, Istok, and Zumba crater and a preliminary analysis on its backweathering rates. Inspiring discussions with Maarten G. Kleinhans and Ernst Hauber greatly improved this paper. Constructive reviews by associate Editor Caleb Fassett and two anonymous reviewers greatly improved this manuscript. We gratefully acknowledge DLR for the use of the HRSC-AX DEM.

References

- André, M.-F. (1997), Holocene rockwall retreat in Svalbard: A triple-rate evolution, *Earth Surf. Processes Landforms*, 22(5), 423–440.
- André, M.-F. (2003), Do periglacial landscapes evolve under periglacial conditions?, *Geomorphology*, 52(1), 149–164.
- Aston, A., S. Conway, and M. Balme (2011), Identifying Martian gully evolution, *Geol. Soc. London Spec. Publ.*, 356(1), 151–169.
- Ballantyne, C. K. (2002a), Paraglacial geomorphology, *Quat. Sci. Rev.*, 21(18), 1935–2017.
- Ballantyne, C. K. (2002b), A general model of paraglacial landscape response, *Holocene*, 12(3), 371–376.
- Ballantyne, C. K., and J. O. Stone (2013), Timing and periodicity of paraglacial rock-slope failures in the Scottish Highlands, *Geomorphology*, 186, 150–161.
- Bandfield, J. L., V. E. Hamilton, and P. R. Christensen (2000), A global view of Martian surface compositions from MGS-TES, *Science*, 287(5458), 1626–1630.
- Banin, A., F. X. Han, I. Kan, and A. Cicelsky (1997), Acidic volatiles and the Mars soil, *J. Geophys. Res.*, 102(E6), 13,341–13,356.
- Bibring, J.-P., et al. (2006), Global mineralogical and aqueous Mars history derived from OMEGA/Mars Express data, *Science*, 312(5772), 400–404.
- Bishop, M. A. (2011), Aeolian scours as putative signatures of wind erosion and sediment transport direction on Mars, *Geomorphology*, 125(4), 569–574.
- Blikra, L. H., and W. Nemec (1998), Postglacial colluvium in western Norway: Depositional processes, facies and palaeoclimatic record, *Sedimentology*, 45(5), 909–960.
- Bourke, M., K. Edgett, and B. Cantor (2008), Recent aeolian dune change on Mars, *Geomorphology*, 94(1–2), 247–255.
- Bridges, N., F. Ayoub, J. Avouac, S. Leprince, A. Lucas, and S. Mattson (2012), Earth-like sand fluxes on Mars, *Nature*, 485(7398), 339–342.
- Bridges, N. T., P. E. Geissler, A. S. McEwen, B. J. Thomson, F. C. Chuang, K. E. Herkenhoff, L. P. Keszthelyi, and S. Martinez-Alonso (2007), Windy Mars: A dynamic planet as seen by the HiRISE camera, *Geophys. Res. Lett.*, 34, L23205, doi:10.1029/2007GL031445.
- Burns, R. G. (1993), Rates and mechanisms of chemical weathering of ferromagnesian silicate minerals on Mars, *Geochim. Cosmochim. Acta*, 57(19), 4555–4574.
- Carr, M. H., and J. W. Head (2010), Geologic history of Mars, *Earth Planet. Sci. Lett.*, 294(3–4), 185–203.
- Cedillo-Flores, Y., A. H. Treiman, J. Lasue, and S. M. Clifford (2011), CO $_2$ gas fluidization in the initiation and formation of Martian polar gullies, *Geophys. Res. Lett.*, 38, L21202, doi:10.1029/2011GL049403.
- Chevrier, V., and P. E. Mathé (2007), Mineralogy and evolution of the surface of Mars: A review, *Planet. Space Sci.*, 55(3), 289–314.
- Church, M., and J. M. Ryder (1972), Paraglacial sedimentation: A consideration of fluvial processes conditioned by glaciation, *Geol. Soc. Am. Bull.*, 83(10), 3059–3072.
- Clark, B. C., and D. C. V. Hart (1981), The salts of Mars, *Icarus*, 45(2), 370–378.

- Conway, S. J., and M. R. Balme (2014), Decameter thick remnant glacial ice deposits on Mars, *Geophys. Res. Lett.*, *41*, 5402–5409, doi:10.1002/2014GL060314.
- Conway, S. J., M. R. Balme, J. B. Murray, M. C. Towner, C. H. Okubo, and P. M. Grindrod (2011), The indication of Martian gully formation processes by slope-area analysis, *Geol. Soc. London Spec. Publ.*, *356*(1), 171–201.
- Costard, F., F. Forget, N. Mangold, and J. P. Peulvast (2002), Formation of recent Martian debris flows by melting of near-surface ground ice at high obliquity, *Science*, *295*(5552), 110–113.
- De Haas, T., E. Hauber, and M. G. Kleinhans (2013), Local Late Amazonian boulder breakdown and denudation rate on Mars, *Geophys. Res. Lett.*, *40*, 3527–3531, doi:10.1002/grl.50726.
- De Haas, T., E. Hauber, S. J. Conway, H. van Steijn, A. Johnsson, and M. G. Kleinhans (2015a), Earth-like aqueous debris-flow activity on Mars at high orbital obliquity in the last million years, *Nat. Commun.*, *6*, 7543, doi:10.1038/ncomms8543.
- De Haas, T., M. G. Kleinhans, P. E. Carbonneau, L. Rubensdotter, and E. Hauber (2015b), Surface morphology of fans in the high-Arctic periglacial environment of Svalbard: Controls and processes, *Earth Sci. Rev.*, *146*, 163–182.
- De Haas, T., D. Ventra, E. Hauber, S. J. Conway, and M. G. Kleinhans (2015c), Sedimentological analyses of Martian gullies: The subsurface as the key to the surface, *Icarus*, *258*, 92–108.
- DiBiase, R. A., A. M. Heimsath, and K. X. Whipple (2012), Hillslope response to tectonic forcing in threshold landscapes, *Earth Surf. Processes Landforms*, *37*(8), 855–865.
- Dickson, J. L., and J. W. Head (2009), The formation and evolution of youthful gullies on Mars: Gullies as the late-stage phase of Mars most recent ice age, *Icarus*, *204*(1), 63–86.
- Dickson, J. L., J. W. Head, and M. Kreslavsky (2007), Martian gullies in the southern mid-latitudes of Mars: Evidence for climate-controlled formation of young fluvial features based upon local and global topography, *Icarus*, *188*(2), 315–323.
- Dickson, J. L., J. W. Head, T. A. Goudge, and L. Barbieri (2015), Recent climate cycles on Mars: Stratigraphic relationships between multiple generations of gullies and the latitude dependent mantle, *Icarus*, *252*, 83–94.
- Douglas, G. (1980), Magnitude frequency study of rockfall in Co. Antrim, N. Ireland, *Earth Surf. Processes Landforms*, *5*(2), 123–129.
- Dundas, C. M., A. S. McEwen, S. Diniega, S. Byrne, and S. Martinez-Alonso (2010), New and recent gully activity on Mars as seen by HiRISE, *Geophys. Res. Lett.*, *37*, L07202.
- Dundas, C. M., S. Diniega, and A. S. McEwen (2014), Long-term monitoring of Martian gully formation and evolution with MRO/HiRISE, *Icarus*, *251*, 244–263.
- Ehlmann, B. L., J. F. Mustard, S. L. Murchie, J.-P. Bibring, A. Meunier, A. A. Fraeman, and Y. Langevin (2011), Subsurface water and clay mineral formation during the early history of Mars, *Nature*, *479*(7371), 53–60.
- Einstein, H., D. Veneziano, G. Baecher, and K. O'reilly (1983), The effect of discontinuity persistence on rock slope stability, *Int. J. Rock Mech. Min. Sci. Geomech. Abstr.*, *20*, 227–236.
- Eppes, M.-C., A. Willis, J. Molaro, S. Abernathy, and B. Zhou (2015), Cracks in Martian boulders exhibit preferred orientations that point to solar-induced thermal stress, *Nat. Commun.*, *6*, 6712.
- Fahey, B. D., and T. H. Lefebvre (1988), The freeze-thaw weathering regime at a section of the Niagara Escarpment on Bruce peninsula, Canada, *Earth Surf. Processes Landforms*, *13*, 293–304.
- Farley, K., et al. (2014), In situ radiometric and exposure age dating of the Martian surface, *Science*, *343*(6169), 1247166.
- Fenton, L. K., A. D. Toigo, and M. I. Richardson (2005), Aeolian processes in Proctor Crater on Mars: Mesoscale modeling of dune-forming winds, *J. Geophys. Res.*, *110*, E06005, doi:10.1029/2004JE002309.
- Gardner, T. W., D. W. Jorgensen, C. Shuman, and C. R. Lemieux (1987), Geomorphic and tectonic process rates: Effects of measured time interval, *Geology*, *15*(3), 259–261.
- Glade, T. (2005), Linking debris-flow hazard assessments with geomorphology, *Geomorphology*, *66*(1), 189–213.
- Golombek, M., et al. (2006), Erosion rates at the Mars Exploration Rover landing sites and long-term climate change on Mars, *J. Geophys. Res.*, *111*, E12S10, doi:10.1029/2006JE002754.
- Golombek, M., C. Bloom, N. Wigton, and N. Warner (2014a), Constraints on the age of Corinto Crater from mapping secondaries in Elysium Planitia on Mars, paper presented at 45th Lunar and Planetary Institute Science Conference Abstracts, held 17–21 March, 2014 at The Woodlands, Tex., p. 1470.
- Golombek, M. P., N. H. Warner, V. Ganti, M. P. Lamb, T. J. Parker, R. L. Fergason, and R. Sullivan (2014b), Small crater modification on Meridiani Planum and implications for erosion rates and climate change on Mars, *J. Geophys. Res. Planets*, *119*, 2522–2547, doi:10.1002/2014JE004658.
- Grindrod, P. M., and N. Warner (2014), Erosion rate and previous extent of interior layered deposits on Mars revealed by obstructed landslides, *Geology*, *42*(9), 795–798.
- Hall, K., C. Thorn, and P. Sumner (2012), On the persistence of 'weathering', *Geomorphology*, *149*, 1–10.
- Hartmann, W. K., and G. Neukum (2001), Cratering chronology and the evolution of Mars, in *Chronology and Evolution of Mars*, edited by R. Kallenbach, J. Geiss, and W. K. Hartmann, pp. 165–194, Springer, Netherlands.
- Hartmann, W. K., C. Quantin, S. C. Werner, and O. Popova (2010), Do young Martian ray craters have ages consistent with the crater count system?, *Icarus*, *208*(2), 621–635.
- Hauber, E., et al. (2011), Landscape evolution in Martian mid-latitude regions: Insights from analogous periglacial landforms in Svalbard, *Geol. Soc. London Spec. Publ.*, *356*(1), 111–131.
- Head, J., M. Kreslavsky, and D. Marchant (2011), Pitted rock surfaces on Mars: A mechanism of formation by transient melting of snow and ice, *J. Geophys. Res.*, *116*, E09007, doi:10.1029/2011JE003826.
- Head, J. W., J. F. Mustard, M. A. Kreslavsky, R. E. Milliken, and D. R. Marchant (2003), Recent ice ages on Mars, *Nature*, *426*, 797–802.
- Hinchliffe, S., and C. K. Ballantyne (1999), Talus accumulation and rockwall retreat, Trotternish, Isle of Skye, Scotland, *Scott. Geogr. Mag.*, *115*(1), 53–70.
- Hoffmann, T., and L. Schrott (2002), Modelling sediment thickness and rockwall retreat in an Alpine valley using 2D-seismic refraction (Reintal, Bavarian Alps), *Z. Geomorphol. Suppl.*, *127*, 153–173.
- Hungr, O., S. Evans, and J. Hazzard (1999), Magnitude and frequency of rock falls and rock slides along the main transportation corridors of southwestern British Columbia, *Can. Geotech. J.*, *36*(2), 224–238.
- Hurowitz, J. A., and S. M. McLennan (2007), A ~3.5 Ga record of water-limited, acidic weathering conditions on Mars, *Earth Planet. Sci. Lett.*, *260*(3–4), 432–443.
- Ivanov, B. A. (2001), Mars/Moon cratering rate ratio estimates, in *Chronology and evolution of Mars*, edited by R. Kallenbach, J. Geiss, and W. K. Hartmann, pp. 87–104, Springer, Netherlands.
- Jagoutz, E. (2006), Salt-induced rock fragmentation on Mars: The role of salt in the weathering of Martian rocks, *Adv. Space Res.*, *38*(4), 696–700.

- Johnsson, A., D. Reiss, E. Hauber, H. Hiesinger, and M. Zanetti (2014), Evidence for very recent melt-water and debris flow activity in gullies in a young mid-latitude crater on Mars, *Icarus*, 235, 37–54.
- Jones, A., A. McEwen, L. Tornabene, V. Baker, H. Melosh, and D. Berman (2011), A geomorphic analysis of Hale crater, Mars: The effects of impact into ice-rich crust, *Icarus*, 211(1), 259–272.
- Kenkmann, T., M. H. Poelchau, and G. Wulf (2014), Structural geology of impact craters, *J. Struct. Geol.*, 62, 156–182.
- Kirk, R., et al. (2008), Ultrahigh resolution topographic mapping of Mars with MRO HiRISE stereo images: Meter-scale slopes of candidate Phoenix landing sites, *J. Geophys. Res.*, 113, E00A24, doi:10.1029/2007JE003000.
- Kneissl, T., S. van Gasselt, and G. Neukum (2011), Map-projection-independent crater size-frequency determination in GIS environments—New software tool for ArcGIS, *Planet. Space Sci.*, 59(11), 1243–1254.
- Krautblatter, M., and R. Dikau (2007), Towards a uniform concept for the comparison and extrapolation of rockwall retreat and rockfall supply, *Geogr. Ann., Ser. A*, 89(1), 21–40.
- Krautblatter, M., and J. R. Moore (2015), Rock slope instability and erosion: Toward improved process understanding, *Earth Surf. Processes Landforms*, 39(9), 1273–1278.
- Krautblatter, M., and M. Moser (2009), A nonlinear model coupling rockfall and rainfall intensity based on a four year measurement in a high Alpine rock wall (Reintal, German Alps), *Nat. Hazards Earth Syst. Sci.*, 9(4), 1425–1432.
- Krautblatter, M., M. Moser, L. Schrott, J. Wolf, and D. Morche (2012), Significance of rockfall magnitude and carbonate dissolution for rock slope erosion and geomorphic work on Alpine limestone cliffs (Reintal, German Alps), *Geomorphology*, 167, 21–34.
- Kumar, P. S., and D. A. Kring (2008), Impact fracturing and structural modification of sedimentary rocks at Meteor Crater, Arizona, *J. Geophys. Res.*, 113, E09009, doi:10.1029/2008JE003115.
- Kumar, P. S., J. W. Head, and D. A. Kring (2010), Erosional modification and gully formation at Meteor Crater, Arizona: Insights into crater degradation processes on Mars, *Icarus*, 208(2), 608–620.
- Malin, M. C. (1974), Salt weathering on Mars, *J. Geophys. Res.*, 79(26), 3888–3894.
- Malin, M. C., and K. S. Edgett (2000), Evidence for recent groundwater seepage and surface runoff on Mars, *Science*, 288(5475), 2330–2335.
- Mangold, N. (2005), High latitude patterned grounds on Mars: Classification, distribution and climatic control, *Icarus*, 174(2), 336–359.
- McCarroll, D., R. A. Shakesby, and J. A. Matthews (2001), Enhanced rockfall activity during the Little Ice Age: Further lichenometric evidence from a Norwegian talus, *Permafrost Periglac. Process.*, 12(2), 157–164.
- McEwen, A. S., B. S. Preblich, E. P. Turtle, N. A. Artemieva, M. P. Golombek, M. Hurst, R. L. Kirk, D. M. Burr, and P. R. Christensen (2005), The rayed crater Zunil and interpretations of small impact craters on Mars, *Icarus*, 176(2), 351–381.
- McFadden, L., M. Eppes, A. Gillespie, and B. Hallet (2005), Physical weathering in arid landscapes due to diurnal variation in the direction of solar heating, *Geol. Soc. Am. Bull.*, 117, 161–173.
- Michael, G. G., and G. Neukum (2010), Planetary surface dating from crater size-frequency distribution measurements: Partial resurfacing events and statistical age uncertainty, *Earth Planet. Sci. Lett.*, 294(3), 223–229.
- Mischna, M. A., M. I. Richardson, R. J. Wilson, and D. J. McCleese (2003), On the orbital forcing of Martian water and CO₂ cycles: A general circulation model study with simplified volatile schemes, *J. Geophys. Res.*, 108(E6), 5062, doi:10.1029/2003JE002051.
- Moore, J. R., J. W. Sanders, W. E. Dietrich, and S. D. Glaser (2009), Influence of rock mass strength on the erosion rate of Alpine cliffs, *Earth Surf. Processes Landforms*, 34(10), 1339–1352.
- Murton, J. B., R. Peterson, and J.-C. Ozouf (2006), Bedrock fracture by ice segregation in cold regions, *Science*, 314(5802), 1127–1129.
- Mustard, J. F., C. D. Cooper, and M. K. Rifkin (2001), Evidence for recent climate change on Mars from the identification of youthful near-surface ground ice, *Nature*, 412(6845), 411–414.
- Nishizumi, K., C. Kohl, E. Shoemaker, J. Arnold, J. Klein, D. Fink, and R. Middleton (1991), In situ 10 Be–26 Al exposure ages at Meteor Crater, Arizona, *Geochim. Cosmochim. Acta*, 55(9), 2699–2703.
- Okubo, C. H., L. L. Tornabene, and N. L. Lanza (2011), Constraints on mechanisms for the growth of gully alcoves in Gasa crater, Mars, from two-dimensional stability assessments of rock slopes, *Icarus*, 211(1), 207–221.
- Pelletier, J. D., K. J. Kolb, A. S. McEwen, and R. L. Kirk (2008), Recent bright gully deposits on Mars: Wet or dry flow?, *Geology*, 36(3), 211–214.
- Phillips, F. M., M. G. Zreda, S. S. Smith, D. Elmore, P. W. Kubik, R. I. Dorn, and D. J. Roddy (1991), Age and geomorphic history of Meteor Crater, Arizona, from cosmogenic ³⁶Cl and ¹⁴C in rock varnish, *Geochim. Cosmochim. Acta*, 55(9), 2695–2698.
- Portyankina, G., A. Pommerol, K.-M. Aye, C. J. Hansen, and N. Thomas (2012), Polygonal cracks in the seasonal semi-translucent CO₂ ice layer in Martian polar areas, *J. Geophys. Res.*, 117, E02006, doi:10.1029/2011JE003917.
- Prager, C., C. Zangerl, G. Patzelt, and R. Brandner (2008), Age distribution of fossil landslides in the Tyrol (Austria) and its surrounding areas, *Nat. Hazards Earth Syst. Sci.*, 8, 377–407.
- Rapp, A. (1960), Talus slopes and mountain walls at Tempelfjorden, Spitsbergen: A geomorphological study of the denudation of slopes in an arctic locality, *Nor. Polarinst. Skri.*, 119, 1–96.
- Reiss, D., S. van Gasselt, G. Neukum, and R. Jaumann (2004), Absolute dune ages and implications for the time of formation of gullies in Nirgal Vallis, Mars, *J. Geophys. Res.*, 109, E06007, doi:10.1029/2004JE002251.
- Reiss, D., et al. (2011), Terrestrial gullies and debris-flow tracks on Svalbard as planetary analogs for Mars, *Geol. Soc. Am. Spec. Pap.*, 483, 165–175.
- Rodriguez-Navarro, C. (1998), Evidence of honeycomb weathering on Mars, *Geophys. Res. Lett.*, 25(17), 3249–3252.
- Sadler, P. (1999), The influence of hiatuses on sediment accumulation rates, *GeoRes. Forum*, 5, 15–40.
- Sadler, P. M. (1981), Sediment accumulation rates and the completeness of stratigraphic sections, *J. Geol.*, 89, 569–584.
- Sass, O. (2005), Spatial patterns of rockfall intensity in the northern Alps, *Z. Geomorphol.*, 138, 51–65.
- Sass, O. (2007), Bedrock detection and talus thickness assessment in the European Alps using geophysical methods, *J. Appl. Geophys.*, 62(3), 254–269.
- Sass, O., and M. Krautblatter (2007), Debris flow-dominated and rockfall-dominated talus slopes: Genetic models derived from GPR measurements, *Geomorphology*, 86(1), 176–192.
- Schon, S. C., and J. W. Head (2012), Gasa impact crater, Mars: Very young gullies formed from impact into latitude-dependent mantle and debris-covered glacier deposits?, *Icarus*, 218(1), 459–477.
- Schon, S. C., J. W. Head, and C. I. Fassett (2009), Unique chronostratigraphic marker in depositional fan stratigraphy on Mars: Evidence for ca. 1.25 Ma gully activity and surficial meltwater origin, *Geology*, 37, 207–210.
- Schon, S. C., J. W. Head, and C. I. Fassett (2012), Recent high-latitude resurfacing by a climate-related latitude-dependent mantle: Constraining age of emplacement from counts of small craters, *Planet. Space Sci.*, 69(1), 49–61.
- Selby, M. (1980), A rock mass strength classification for geomorphic purposes: With tests from Antarctica and New Zealand, *Z. Geomorphol.*, 24(1), 31–51.

- Siewert, M. B., M. Krautblatter, H. H. Christiansen, and M. Eckerstorfer (2012), Arctic rockwall retreat rates estimated using laboratory-calibrated ERT measurements of talus cones in Longyearfjorden, Svalbard, *Earth Surf. Processes Landforms*, 37(14), 1542–1555.
- Söderman, G. (1980), Slope processes in cold environments of northern Finland, *Fennia*, 158(2), 83–152.
- Squyres, S. W., et al. (2009), Exploration of Victoria crater by the Mars rover Opportunity, *Science*, 324(5930), 1058–1061.
- Sutton, S. (1985), Thermoluminescence measurements on shock-metamorphosed sandstone and dolomite from Meteor Crater, Arizona: 2. Thermoluminescence age of Meteor crater, *J. Geophys. Res.*, 90(B5), 3690–3700.
- Tanaka, K., J. Skinner, J. Dohm, R. Irwin III, E. Kolb, C. Fortezzo, T. Platz, G. Michael, and T. Hare (2014), Geologic map of Mars, *Tech. Rep.*, U.S. Geological Survey Scientific Investigations Map 3292, U.S. Geol. Surv., Flagstaff, Arizona.
- Thomas, M., J. D. A. Clark, and C. F. Pain (2005), Weathering, erosion and landscape processes on Mars identified from recent rover imagery, and possible Earth analogues, *Aust. J. Earth Sci.*, 52, 365–378.
- Treiman, A. H. (2003), Geologic settings of Martian gullies: Implications for their origins, *J. Geophys. Res.*, 108(E4), 8031, doi:10.1029/2002JE001900.
- Viles, H., B. Ehlmann, C. Wilson, T. Cebula, M. Page, and M. Bourke (2010), Simulating weathering of basalt on Mars and Earth by thermal cycling, *Geophys. Res. Lett.*, 37, L18201, doi:10.1029/2010GL043522.
- Viles, H. A. (2001), Scale issues in weathering studies, *Geomorphology*, 41(1), 63–72.
- Viles, H. A. (2013), Linking weathering and rock slope instability: Non-linear perspectives, *Earth Surf. Processes Landforms*, 38(1), 62–70.
- Wang, X., L. Luo, H. Guo, L. Mu, C. Li, W. Ji, and H. Cai (2013), Cratering process and morphological features of the Xiuyan impact crater in Northeast China, *Sci. China Earth Sci.*, 56(10), 1629–1638.
- Warke, P. A. (2013), Weathering in arid regions, in *Treatise on Geomorphology, Weathering and Soils Geomorphology*, vol. 4, edited by J. Shroder and G. A. Pope, pp. 197–227, Academic Press, San Diego, Calif.
- Whalley, W. B. (1974), *The Mechanics of High-Magnitude, Low-Frequency Rock Failure and Its Importance in a Mountainous Area*, *Geog. Pap.*, vol. 27, Univ. of Reading, Dept. of Geog., Reading, U. K.
- Williams, K., O. Toon, J. Heldmann, and M. Mellon (2009), Ancient melting of mid-latitude snowpacks on Mars as a water source for gullies, *Icarus*, 200(2), 418–425, doi:10.1016/j.icarus.2008.12.013.